Available online at www.sciencedirect.com
SCIENCE DIRECT
Journal of Asian Earth Sciences 26 (2006) 555–574
Journal of Asian Earth Sciences
www.elsevier.com/locate/jaes

Pressure–temperature-deformation history for a part of the Mesoproterozoic fold belt in North Singhbhum, Eastern India

Manua Ghosh[a,*], Dhruba Mukhopadhyay[b], Pulak Sengupta[c]

[a]Department of Geology and Geophysics, Indian Institute of Technology, Kharagpur 721302, India
[b]Department of Geology, University of Calcutta, 35 Ballygunge Circular Road, Calcutta 700 019, India
[c]Department of Geological Sciences, Jadavpur University, Calcutta 700032, India

Received 15 October 2003; revised 22 October 2004; accepted 3 November 2004

Abstract

The supracrustal rocks in the easternmost part of the Proterozoic fold belt of North Singhbhum, eastern India, are folded into a series of large upright folds with variable plunges. The regional schistosity is axial–planar to the folds. The folds were produced by a second phase of deformation (D2) and were preceded by D1 deformation, which gave rise to isoclinal folds (mapped outside the study area) and the locally preserved, bedding-parallel schistosity. A shearing deformation during D2 was responsible for the sheath-like geometry of a major fold. The axial planes were curved by D3 warping. The first metamorphic episode (M1) of low-pressure type produced andalusite porphyroblasts prior to, or in the early stage of, D1 deformation. The main metamorphism (M2), responsible for the formation of chloritoid, kyanite, garnet and staurolite porphyroblasts, was late- to post-D2 in occurrence. The Staurolite isograd separates two zonal assemblages recorded in the high-alumina and the low-alumina pelitic schists. Geothermobarometric calculations indicate the peak metamorphic temperature to be 550 °C at 5.5 kb. Fluid composition in the rocks before and during M2 metamorphism was buffered and fluid influx, if any, was not extensive enough to overcome the buffering capacity of the rocks. From M1 to M2, the *P–T* path is found to have a clockwise trajectory, that is consistent with a tectonic model involving initial asthenospheric upwelling and rifting, followed by compressional deformation leading to loading and heating.

Keywords: Proterozoic fold belt; Deformation and metamorphism; *P–T* trajectory; Rifting and orogenesis

1. Introduction

The Indian shield, a part of Gondwanaland, is made up of two continental blocks—the southern Dharwar–Bastar–Singhbhum block and the northern Bundelkhand block—that were amalgamated during Mesoproterozoic time; their junction is referred to as the Central Indian Tectonic Zone (CITZ, Fig. 1) (Radhakrishna and Ramakrishnan, 1988; Yedekar et al., 1990; Jain et al., 1995). The CITZ has linear continuity with the Albany–Fraser mobile belt of Australia in the reconstructed Gondwanaland (Harris, 1993; Harris and Beeson, 1993; Yoshida, 1995). Recent work has demonstrated that in central India, the CITZ is an ensemble of different tectono-metamorphic belts, that had been assembled together during Meso- to Neo-proterozoic time (Roy and Hanuma Prasad, 2003; Acharyya, 2003). Eastward, the CITZ continues north of the Archaean nucleus of Singhbhum (Mukhopadhyay, 2001), and is represented by the North Singhbhum Fold Belt (NSFB). This is followed further north by the Chotonagpur Gneiss Terrane. Further east, the Ganga–Brahmaputra alluvial plain covers the CITZ. It has been surmized that the Precambrian terrane of the Shillong Plateau represents the eastern extension of the CITZ (Acharyya, 2003), but the evidence is equivocal.

The NSFB has a thick sequence of metamorphosed pelitic, psammitic and volcaniclastic rocks belonging to the Chaibasa and Dhalbhum Formations of the Singhbhum Group (Sarakar and Saha, 1962). Available geochronological data suggest the age of metamorphism to be 1600—1800 Ma (KrishnaRao et al., 1979; Sarkar et al., 1986; Sengupta et al., 1994; Sengupta and Mukhopadhyay, 2000). This study, which covers a part of the eastern extremity of the fold belt near the small town of Dhalbhumgarh

* Corresponding author. Tel.: +91 3222 277435.
E-mail address: manuaghosh64@yahoo.co.in (M. Ghosh).

1367-9120/$ - see front matter © 2005 Elsevier Ltd. All rights reserved.
doi:10.1016/j.jseaes.2004.11.007

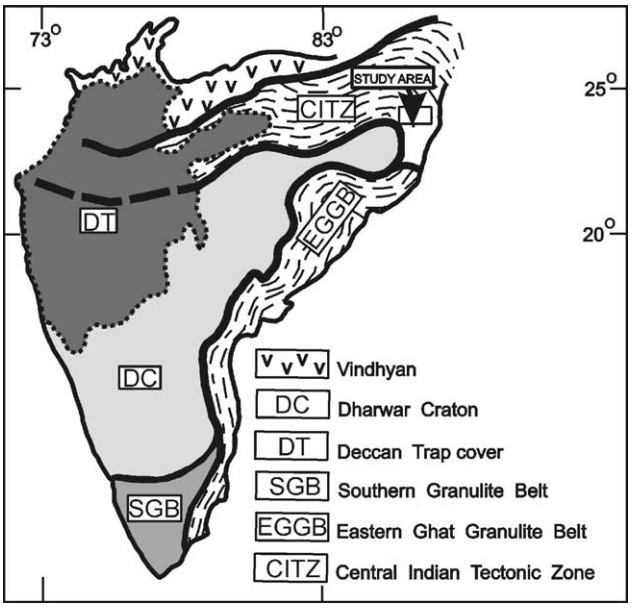

Fig. 1. Location of the study-area within the geotectonic framework of India (modified from Radhakrishna and Naqvi, 1986).

(latitudes 22°29′N–22°40′N and longitudes 86°30′E–86°45′E), records the pressure–temperature-deformation history of rocks in this area and suggests a tectonic model for the evolution of the fold belt.

Earlier studies in a neighbouring part of the fold belt (Sarakar and Saha, 1962; Naha, 1965) established the presence of E–W regional folds with axial planar schistosity and variably plunging fold axes. Metamorphism was reported by Naha (1965) to be of Barrovian type, reaching staurolite and kyanite zones. It was broadly synchronous with, but outlasted, the deformation event responsible for the development of the regional schistosity.

2. Structural pattern

The large scale structural pattern of the study area is marked by a series of folds with subvertical curved axial surfaces and steeply plunging axes (Fig. 2). The regional schistosity is axial planar to the folds. These folds are correlatable with major folds in the Ghatshila—Galudih region (Fig. 3) to the west, interpreted as first generation

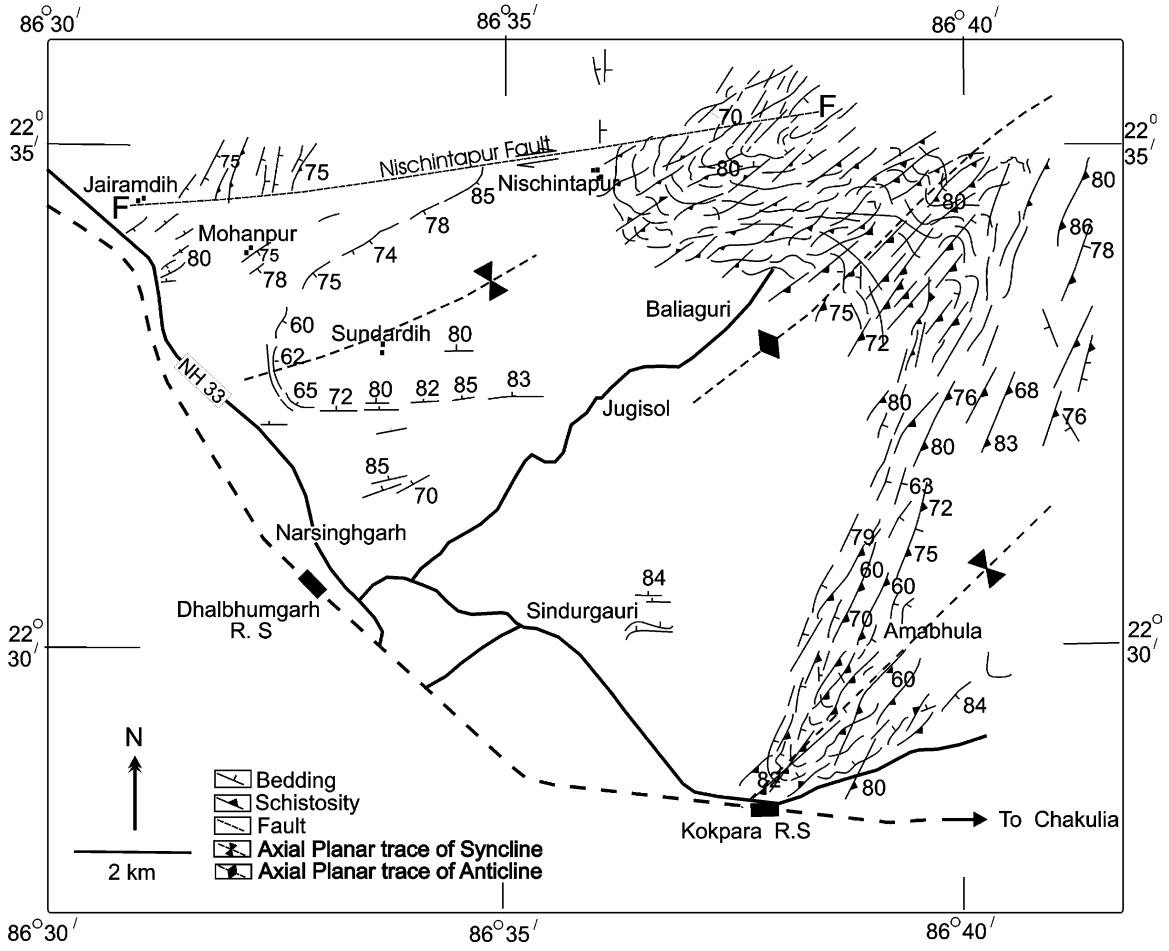

Fig. 2. Structural map of the Dhalbhumgarh area. Some data in the northeastern part of the area are taken from Chattopadhyay (1990).

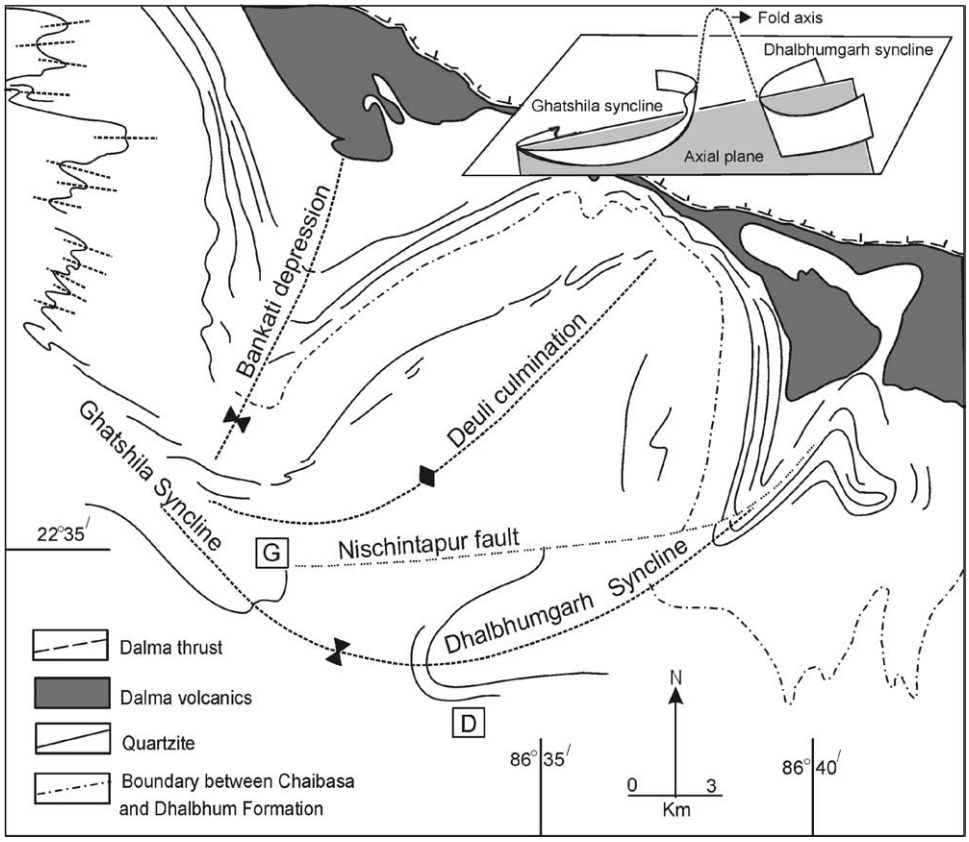

Fig. 3. Geological map of the Ghatshila–Galudih–Dhalbhumgarh area. G, Ghatshila; D, Dhalbhumgarh (modified from Sarakar and Saha, 1962, with additional data from Mukhopadhyay and Sengupta, 1971; Chattopadhyay, 1990 and the present work). Area shown in Fig. 2 occupies the southeastern corner. Inset shows a three-dimensional representation of the Ghatshila–Dhalbhumgarh sheath fold.

structures by Naha (1965), and with folds of the Simulpal region further east which were mapped as second generation structures by Mukhopadhyay and Sengupta (1971). The U-shaped synclinal fold closures at Dhalbhumgarh and at Ghatshila (Fig. 3) face in opposite directions and have steep easterly and westerly plunges, respectively, defining an acute culmination of the axis. Further to the west, a plunge depression on the same axial trace has given rise to a canoe-shaped fold near Ghatshila (Naha, 1965). This culmination and depression define the overall geometry of the Dhalbhumgarh—Ghatshila syncline as a sheath-like fold (Fig. 3, inset).

The major folds of the study area and the axial planar schistosity belong to the second phase of deformation (D2) (cf. Mukhopadhyay and Sengupta, 1971). The imprints of an earlier deformational phase are preserved as small-scale, rootless, isoclinal folds defined by quartzose lenticles in schists. Thin micaceous laminae in some schists show bedding-parallel D1 schistosity that is crenulated; the axial planar crenulation cleavage continues in the more quartzose bands as anastomosing, disjunctive schistosity defined by subparallel alignment of flaky minerals (Fig. 4a). In some micaceous schists, the regional D2 schistosity can be identified as a crenulation cleavage, which has almost completely transposed the earlier, tightly folded D1 schistosity.

The D2 schistosity is folded by D3 crenulations that have variable attitudes of axes and axial planes. The broad curvature of the axial traces of the D2 major folds owes itself to a large D3 structure (Fig. 3) that has been demarcated as the Banakati Depression by Sarakar and Saha (1962).

The D2 planar fabric has the appearance of proto-mylonitic to mylonitic foliation (Fig. 4b) in some quartzites and schists. Shear planes and shear bands (C' planes) cut across this fabric and cause a sigmoidal curvature of the latter. Within some shear bands in phyllonites, the main foliation is dragged into parallelism with the boundaries of the bands. This foliation within the shear bands is crenulated by D3, establishing that the shearing pre-dated D3. The parallelism of the mylonitic foliation with the D2 fabric leads us to infer that the shearing movement took place during the late stage of D2 deformation. The sheath-like geometry of the D2 folds is attributed to this shearing movement on the schistosity planes (Mukhopadhyay et al., 2004).

The shearing had a thrust sense of movement (top-to-the-south) and rotated the fold axes towards the direction of transport. We interpret that the shortening and simple shear deformation were together responsible for the evolution of the structural pattern in the NSFB (Mukhopadhyay et al., 2004). A model of thrust stacking has been proposed for the NSFB (Sengupta and Mukhopadhyay, 2000).

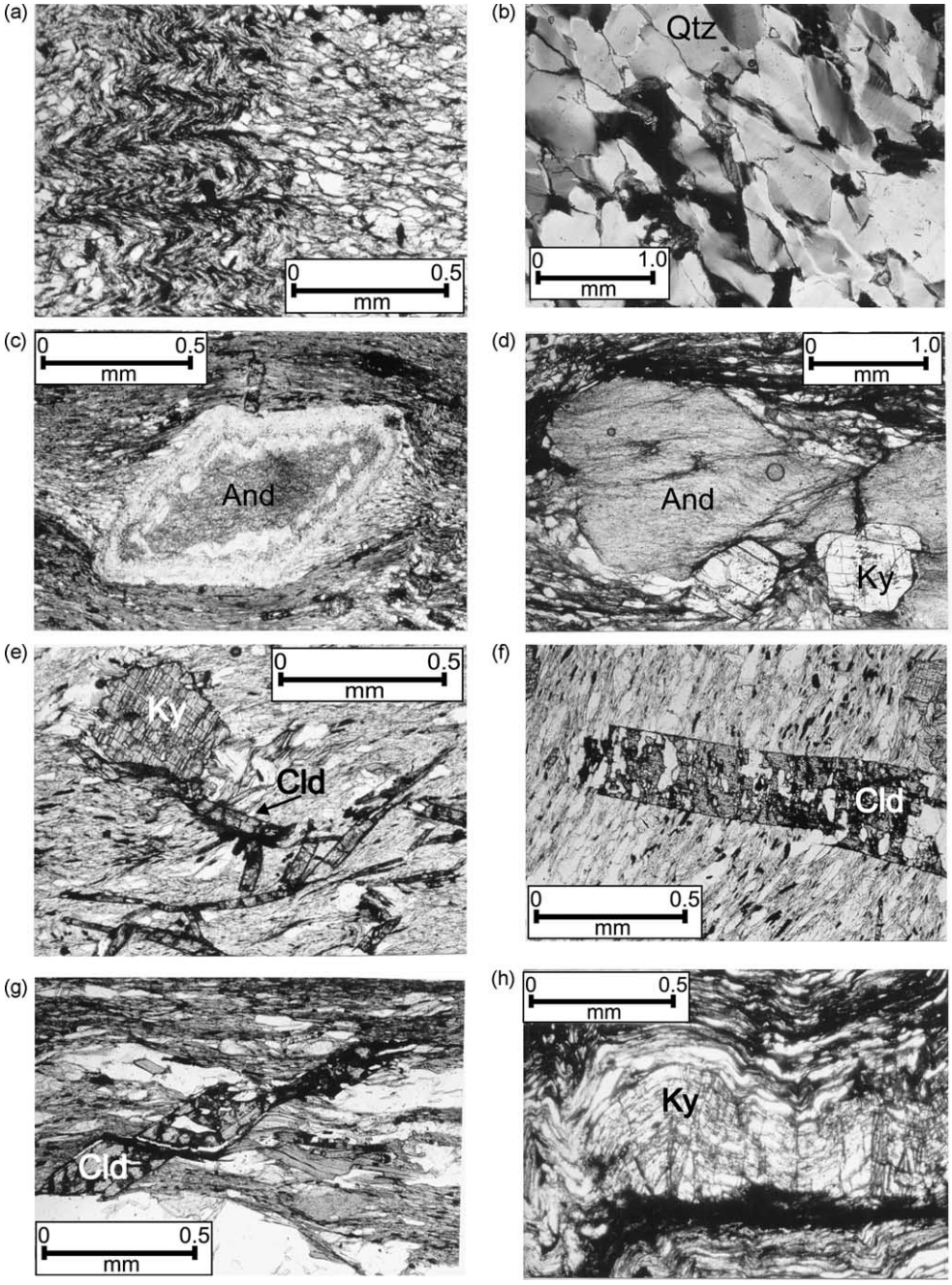

Fig. 4. Textural relations in High Aluminous Pelitic- and Low Aluminous Pelitic-schists. (a) D2 crenulation cleavage in micaceous laminae transforming into disjunctive cleavage in quartzose layer. (b) Protomylonitic foliation parallel to the D2 axial plane in quartzite. (c) Altered andalusite porphyroblast with internal zonation and with a chloritic core. (d) D2 schistosity superimposed on a micaceous aggregate within an andalusite pseudomorph. Shear plane cuts across the pseudomorph. Note unaltered kyanite porphyroblast penetrating into the pseudomorph. (e) Disoriented chloritoid and kyanite porphyroblasts growing over D2 schistosity. (f) Chloritoid porphyroblast growing over D2 schistosity. Straight inclusion trails in chloritoid are parallel to external schistosity. (g) Chloritoid blade displaced by slip on D2-schistosity surface. (h) Kyanite porphyroblast kinked by D3 folds. (i) Chloritoid crystal penetrating into andalusite pseudomorph. Kyanite grains also occur within and outside the pseudomorph. (j) Garnet with sigmoidal inclusion trails enclosed within staurolite with straight inclusion trails. Note the difference in size of inclusions within staurolite and garnet. (k) Staurolite with folded helicitic inclusion trails. (l) Planar inclusion-free and inclusion-rich zones within staurolite. Folded helicitic trails are present within the inclusion-rich zone (marked by bold white line). Axial planes of folds are parallel to the boundary between the zones.

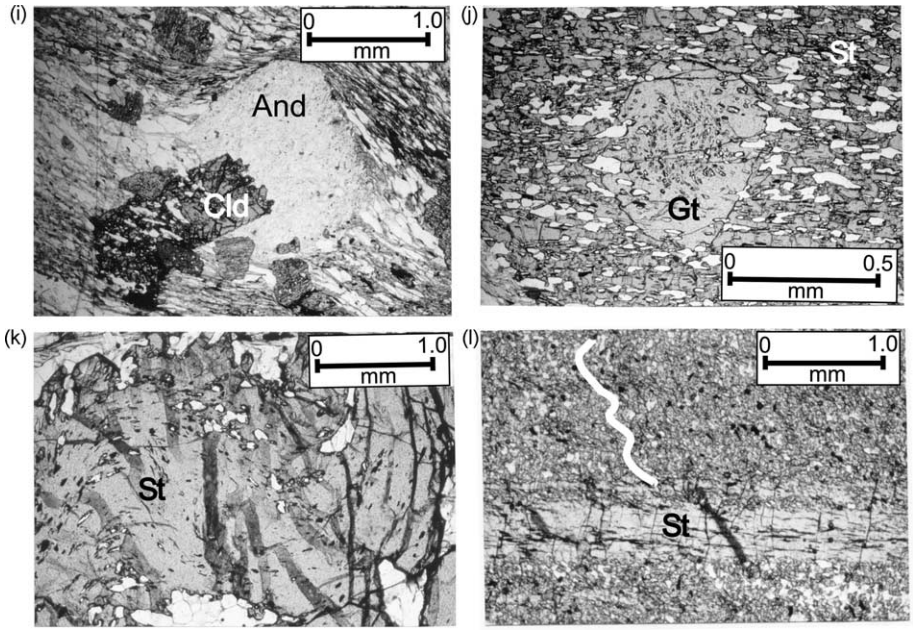

Fig. 4 (*continued*)

3. Mineral assemblages and textural relations

3.1. General

Pelitic schists occupy a major part of the study area, and are of two types: (a) biotite-free, chloritoid-bearing schists containing andalusite–kyanite, referred to here as the high aluminous pelitic schists or HAP schists, and (b) biotite-bearing, chloritoid-free schists lacking aluminosilicates, referred to here as the low aluminous pelitic schists or LAP schists. Some transitional varieties and some varieties with calcareous material are also found.

Petrographic studies indicate that two distinct phases of prograde metamorphism affected the rocks, the main metamorphism being M2. The significant mineral assemblages in the two types of pelitic schists are given in Table 1; the assemblages also contain quartz, muscovite, opaques (ilmenite and magnetite) and small amounts of plagioclase. The AFM minerals belonging to the M2 metamorphic phase are indicated in italics in the table and are plotted in Fig. 5.

Table 1
Mineral assemblages in the different rock types

Rock type	Mineral assemblages	No. of thin sections
A. HAP Schist	Kyanite–chloritoid zone (M2)	
1.	*Chlorite* + *chloritoid* + *kyanite* + andalusite + / − plagioclase	57
2.	*Chlorite* + *kyanite* + / − andalusite	32
B.	Staurolite–garnet–chlorite zone (M2)	
3.	*Chlorite* + *garnet* + *staurolite*	21
4.	*Chlorite* + / − *kyanite* + *staurolite* + / − andalusite	25
5.	*Chlorite* + *garnet* + / − epidote	6
6.	*Chlorite* + *kyanite* + *staurolite* + *chloritoid*	1
C. LAP Schist	Garnet–chlorite–biotite zone (M2)	
7.	*Chlorite* + *biotite* + / − plagioclase	20
8.	*Chlorite* + *biotite* + *garnet* + / − plagioclase	45
D.	Staurolite–biotite zone (M2)	
9.	*Biotite* + *garnet* + *staurolite* + / − plagioclase	7
10.	*Biotite* + *garnet* + *staurolite* + *chlorite* + / − plagioclase	42
E[a]. Pelitic schist with	Garnet–biotite zone (M2)	
11. Calcareous impurities	*Chlorite* + *biotite* + / − plagioclase + epidote + carbonate	6
F[a]	Staurolite–biotite zone (M2)	
12.	*Chlorite* + *biotite* + *garnet* + *staurolite* + plagioclase + epidote + carbonate + / − K-feldspar	10

Samples in HAP Schist: Kp7, Kp20, Kp88, K65. Samples in LAP Schist: Kp62, Kp99, Kp73, A817, Dh20. Samples in Impure Carbonate rock: Kp80, Kp95. Samples in Metabasic rock: A810, Dh18.

[a] The assemblages are without muscovite or with only subordinate amount of muscovite. M2 phases are shown in italics.

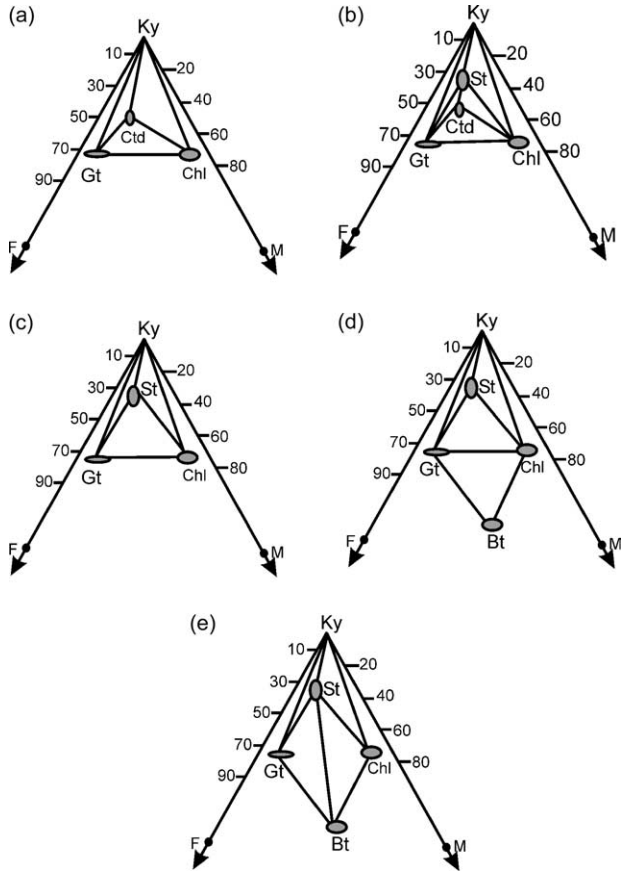

Fig. 5. AFM diagrams representing M2 assemblages in HAP and LAP schists. (a) Kyanite–chloritoid zone assemblages in HAP schists. (b) Staurolite–garnet–chlorite zone assemblages in HAP schists after the breakdown of the chloritoid–kyanite tie-line. (c) Staurolite–garnet–chlorite zone assemblages in HAP schists after the terminal breakdown of chloritoid. (d) Staurolite–garnet–chlorite assemblage in HAP schists and garnet–chlorite–biotite assemblage in LAP schists. (e) Staurolite–biotite zone assemblages in LAP schists.

HAP and LAP assemblages correspond to bulk compositions falling above and below the garnet–chlorite join, respectively. The M2 assemblages belong to two zones separated by the staurolite isograd. The spatial distribution of the assemblages is shown in Fig. 6.

3.2. Mineral growth in relation to deformation

In both LAP and HAP schists, muscovite and chlorite generally occur as interwoven aggregates, the flakes being parallel to both D1 and D2 schistosity. Later porphyroblasts of these minerals lying oblique to the D2 fabric are kinked owing to D3 deformation. Clots of secondary chlorite flakes have been produced by retrogression of garnet and chloritoid. Some large porphyroblasts of chlorite contain pleochroic halos, which are similar to those seen in biotite porphyroblasts; these appear to be retrogressive products of biotite. Thus the crystallization of muscovite and chlorite continued all through D1, D2 and post-D2 stages.

Biotite, which is exclusive to the LAP schists and the transitional and calcareous varieties, is parallel to the D2 schistosity and cuts across the D1 muscovite flakes. These are syntectonic with respect to D2, although post-D2 stumpy porphyroblasts, often kinked by D3, are also present.

Andalusite porphyroblasts, often in euhedral dipyramidal crystal-forms with orthorhombic symmetry, are invariably altered to pseudomorphs of fine-grained micaceous aggregates (*shimmer aggregate*), made up of ephesite and paragonite. The D2 schistosity curves around the porphyroblasts. The crenulated D1 schistosity is at places preserved in the well-developed pressure shadow zones, while in the matrix the D1 fabric is completely transposed by D2 schistosity. Rows of dusty opaque grains arranged subparallely to crystal boundary, indicate relict zoning in some altered porphyroblasts. Many of these pseudomorphs have chlorite-rich cores (Fig. 4c); the chloritic aggregate either does not display any planar fabric or shows a crudely developed fabric. We interpret that the cores represent the matrix of the rock incorporated during the growth of andalusite. The textural evidence indicates that andalusite crystallized in a low grade (chlorite–muscovite) matrix, prior to or at an early stage of the deformation. The preservation of crystal outlines suggests that during the D2 deformation, andalusite existed as relatively rigid porphyroblasts in a deforming matrix. The alteration to micaceous aggregate must have taken place after the peak D2 deformation event; otherwise the micaceous pseudomorphs could not have retained the euhedral form. However, the elongated lenticular shape of some pseudomorphs, the development of schistose fabric within some of the micaceous aggregates (Fig. 4d) and the occasional presence of asymmetrical sigmoidal tails together indicate that the late stage of D2 deformation and the shearing continued after the alteration.

Chloritoid occurs in HAP schists as long slender grains or stumpy porphyroblasts superimposed on the D2 schistosity (Fig. 4e); these have inclusion trails parallel to the external schistosity (Fig. 4f). Some grains are broken and displaced parallel to the D2 schistosity (Fig. 4g), and long chloritoid flakes parallel to the schistosity are kinked and bent by D3 deformation. At places, chloritoid has partially penetrated into the andalusite pseudomorphs (Fig. 4i). Thus, the crystallization of chloritoid is post-D2-schistosity but is pre-D2-shearing and pre-D3; it is later than the alteration of andalusite. Some chloritoid grains have inclusions of chlorite in the core, and in rare instances chloritoid is pseudomorphed by aggregates of chlorite.

Kyanite crystals in HAP schists and quartzites have grown over the D2-schistosity (Fig. 4e), but are found to have been kinked during folding of schistosity by D3 (Fig. 4h). Kyanite blades have grown within the andalusite pseudomorphs (*shimmer aggregates*) (Fig. 4d and i). Where the kyanite porphyroblast extends from the matrix into pseudomorph, the part of kyanite within the matrix is riddled with inclusions but the part extending into

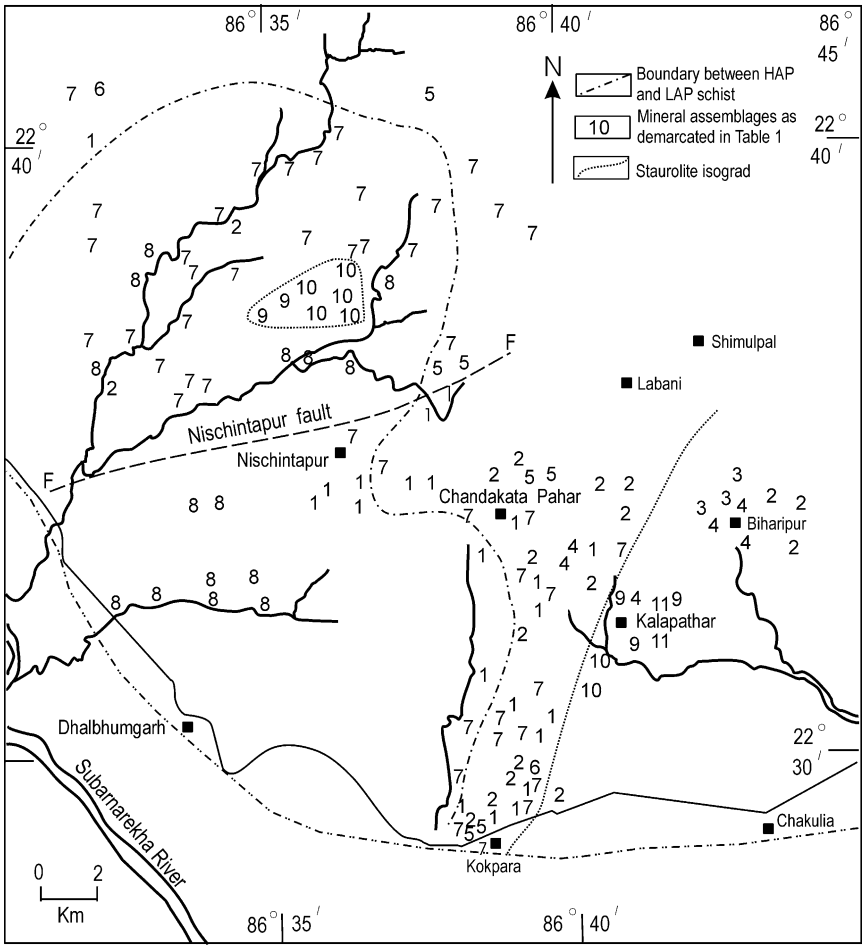

Fig. 6. Map showing the areal distribution of mineral assemblages in the study area. Area in Fig. 2 occupies the southern half of this area.

the pseudomorph is clear; in some grains rows of dusty opaque grains defining zones within the pseudomorphs continue uninterrupted within the penetrating kyanite (Fig. 7a and b). Kyanite is pre-D3, but post-D2, and is later than the alteration of andalusite.

D2 schistosity typically curves around garnet porphyroblasts, most of which do not show any inclusion trails. A few grains show helicitic inclusion trails of folded D1 schistosity, while in the matrix only planar D2 schistosity is seen (Passchier and Trouw, 1996). Garnet included within staurolite shows sigmoidal trails of very fine-grained inclusions, while in the enclosing staurolite the inclusion trails defined by larger quartz grains are straight and continuous with the external D2 schistosity (Fig. 4j). Where the rock fabric is mylonitic, garnet is pre-mylonitization; this is indicated by the fact that quartz grains within the garnet show no strain effect, whereas those outside the garnet crystal are highly strained and reduced to a fine grainsize. Thus crystallization of garnet is syn- to post-tectonic with respect to D2 folding but is earlier than D2 shearing.

Staurolite in HAP and LAP schists occurs as porphyroblasts (up to 15 cm in length) with straight inclusion trails defined by relatively large quartz grains. The trails are continuous with the external D2 schistosity. In some porphyroblasts helicitic, folded trails of D1 schistosity are defined by fine-grained inclusions (Fig. 4k), while in the matrix only planar D2 schistosity is seen. At places alternating, parallel, inclusion-free, and inclusion-rich bands are present within staurolite; the inclusion-rich bands have folded helicitic trails (Fig. 4l). This indicates that staurolite is post-D2 and it grew in a matrix with differentiated D2 crenulation cleavage containing mica-rich and mica-poor domains (Passchier and Trouw, 1996). The crystallization of staurolite is pre-D3, as evidenced by straight inclusion trails within staurolite grains while the external D2 schistosity is crenulated.

3.3. Mineral composition

A summary of the chemical data is given in Appendix A. Some cardinal points about the compositional data are highlighted here.

The muscovite flakes parallel to the schistosity are rich in the muscovite end-member, paragonite being the second dominant component. The mole fractions of other components are negligible. They are slightly phengitic, with the maximum value of $Si:Al^{vi}$ reaching 3.865. The athwart

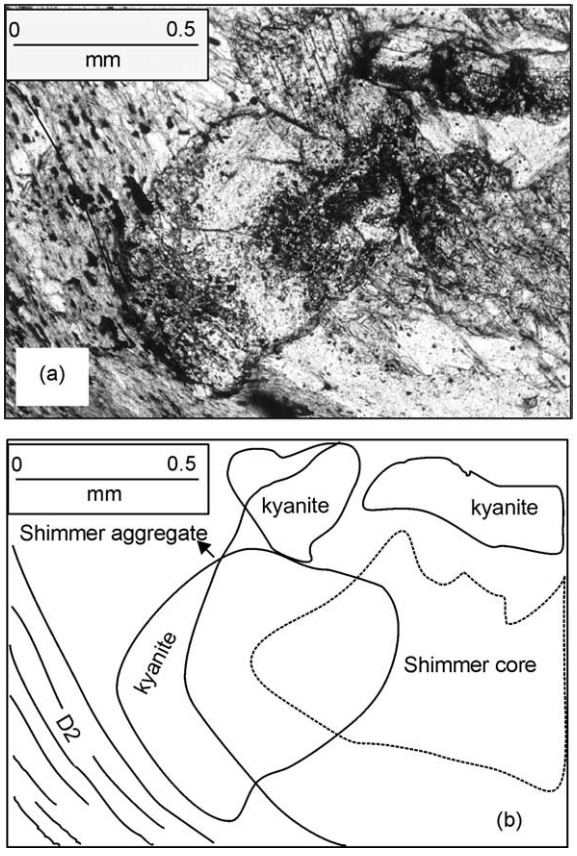

Fig. 7. (a) Kyanite growing over andalusite pseudomorph. Zones in andalusite continue as inclusion defined zones in kyanite. (b) Explanatory sketch of Fig. 7a.

porphyroblasts of muscovite are richer in paragonite content, and the paragonite content increases in the rim relative to the core.

Chlorites fall in the ripidolite field of Hey's (1994) classification and in the pelitic field of Spear's (1993) quadrilateral plot. Fe/Mg ratio decreases in the higher grade assemblages.

Chloritoid is found only in the HAP schists. It is an iron rich variety, and the Fe/Mg ratio is much higher than in the coexisting chlorite.

Phlogopite–annite is the dominant constituent in biotite. The subordinate constituents are muscovite, eastonite–siderophyllite, and in one sample, talc–minnesotite. The Fe/Mg ratio decreases in the higher grade rocks.

Garnets are all almandine-rich and there is very little variation in composition from core to rim. This is probably due to homogenization as a result of volume diffusion at the peak temperature (Tracy, 1982). The Fe/Mg ratio, as well as the spessartite content, decrease in the higher grade rocks. The garnets from the calcareous pelites have lower almandine content, much higher spessartite content and slightly higher grossularite content. Their high Mn-content is a reflection of the bulk composition of the rock.

Staurolites are iron-rich. Large equant, octahedral, opaque grains commonly found in many HAP schists are primarily magnetite, while the slender opaque needles in both HAP and LAP schists are ilmenite.

4. Reaction equilibria

4.1. M1 metamorphism

In the high-alumina pelites, the first phase of metamorphism (M1) produced andalusite porphyroblasts in a matrix of quartz, chlorite and muscovite. The stabilization of andalusite may be modelled after the reactions

pyrophyllite = andalusite + quartz + H_2O

paragonite + quartz = andalusite + muscovite + albite + H_2O (Holland, 1979; Okuyama-Kusunose, 1994)

As indicated by inclusions in the core of andalusite, the original clay minerals smectite, kaolinite and illite, were converted to chlorite and muscovite by the time andalusite formed.

The late- to post-D2 decomposition of andalusite to *shimmer aggregate* is considered to have been produced by a model reaction of the type

andalusite + H_2O + Na^+ = ephesite + paragonite,

involving hydration with introduction of Na^+into the system.

4.2. M2 metamorphism

The main phase of regional metamorphism (M2) produced chloritoid, kyanite, garnet and staurolite porphyroblasts, and the peak of M2 metamorphism post-dated D2 deformation.

The mineral assemblages within the HAP schists belong to two principal zones: kyanite–chloritoid zone and staurolite–garnet–chlorite zone. The corresponding zones in LAP schists are garnet–biotite–chlorite zone and staurolite–garnet–biotite zone. The two zones are separated by the staurolite isograd.

Presence of chlorite and magnetite inclusions in chloritoid suggests the following model reactions:

Fe-chlorite + pyrophyllite = Fe-chloritoid + quartz + H_2O (Miyashiro, 1973; Spear, 1993)

pyrophyllite + magnetite = chloritoid + quartz + H_2O + O_2

Fe-chlorite + hematite = chloritoid + magnetite + quartz + H_2O (Thompson and Norton, 1968)

The textural relations give no clue to the specific reaction responsible for the production of low grade kyanite in the HAP schists. It is later than the D2 schistosity and presumably developed by reactions

involving schistosity-defining minerals, muscovite and chlorite. Two possible reactions are:

muscovite + chlorite(1) + quartz = kyanite + chlorite(2) + phengite (Kruhl, 1993)
pyrophyllite = kyanite + H_2O (Kerrick, 1968, Chatterjee et al., 1984)

The following 'ionic reactions' may also be proposed for the andalusite → kyanite transformation (cf. Carmichael, 1969):

andalusite + quartz + (K^+, Na^+) + H_2O = white mica + H^+
white mica + H^+ = kyanite + quartz + (K^+, Na^+) + H_2O

Kerrick (1990) questioned the applicability of Carmichael's (1969) ionic model to natural rocks on the ground that textures supporting the breaking and making of Al_2SiO_5 polymorphs were not present in the rocks. However, the textural features observed in the study area lend support to Carmichael's model that the two coupled reactions mentioned above may be responsible for the formation of kyanite, driven by the Gibbs free energy change for the reaction andalusite → kyanite during M2 metamorphism.

Garnet growth in the HAP schists, following the stabilization of the chlorite–chloritoid–kyanite assemblage, may be accounted for by the reaction

chloritoid + chlorite + quartz = garnet + H_2O (Thompson and Norton, 1968)

The exact *P–T* location of this reaction is not known, but the areal distribution of the assemblages in the area suggest that garnet first appeared at a temperature not much lower than the stabilization of staurolite in the HAP schists.

Inclusions of chlorite and biotite in garnet from the chloritoid-absent LAP schists, and the presence of post-schistosity biotite suggest the following reactions for the formation of garnet:

chlorite + quartz = garnet + H_2O (Thompson and Norton, 1968, Wang and Spear, 1991)
chlorite + muscovite + quartz = garnet + biotite + H_2O (Thompson and Norton, 1968, Yardley, 1988)
chlorite + biotite(1) + quartz = garnet + biotite(2) + H_2O (Chakraborty and Sen, 1967)

The AFM assemblages after the stabilization of chloritoid and kyanite in HAP schists are given in Fig. 5a.

The first appearance of staurolite in the HAP schists is linked with the disappearance of chloritoid:

chloritoid + kyanite = staurolite + quartz + H_2O (Hoschek, 1967)
chloritoid + kyanite + quartz = staurolite + chlorite + H_2O (Spear, 1993)

Hoschek's estimate of a temperature of 545 °C and 4 kb pressure for the first reaction is not much different from Ganguly's (1969) experimental determination. The second reaction is of 'tie-line-flip' type in the KFMASH system, and is believed by Spear (1993) to be responsible for the first appearance of staurolite and disappearance of chloritoid + kyanite in high alumina pelites (Fig. 5b). This reaction also explains the growth of post-D2 chlorite in the rocks. As a result of these reactions, the kyanite–chloritoid–chlorite assemblage is followed by the staurolite–kyanite–chlorite assemblage. The following reaction takes place at a slightly (15–30 °C) higher temperature than the first reaction

chloritoid + quartz = staurolite + almandine + H_2O (Ganguly, 1969)

Finally, at a still higher temperature, the terminal stability reaction in the KFMASH system takes place:

chloritoid = staurolite + garnet + chlorite (Spear, 1993)

This leads to the stabilization of the assemblage garnet–staurolite–chlorite (Fig. 5c). This assemblage is common in the staurolite zone in the HAP schists of the present area. Inasmuch as magnetite is a common constituent in HAP schists, the following redox reaction could also be responsible for the appearance of staurolite

chloritoid + O_2 = staurolite + magnetite + SiO_2 + H_2O (Ganguly, 1968)
chloritoid + kyanite + magnetite = staurolite + quartz + O_2 (Ganguly, 1968)

In absence of chloritoid, staurolite is likely to have formed in the LAP schists through other reactions involving chlorite and garnet

chlorite + muscovite = staurolite + biotite + quartz + H_2O (Hoschek, 1969)
chlorite + muscovite + garnet = staurolite + biotite + quartz + H_2O (Carmichael, 1970)

The topology of the AFM diagrams (Fig. 5d and e) shows that stabilization of the staurolite + biotite assemblage in the LAP schists takes place at a higher grade than the appearance of staurolite in the HAP schists (Fig. 5c). It may be noted that all staurolite-forming reactions in pelites occur within a narrow temperature interval (Ganguly, 1968, 1969; Spear, 1993) and the appearance of staurolite can be taken to practically mark an isograd. One HAP sample from this area shows a four-phase assemblage (kyanite + staurolite + chloritoid + chlorite) which in the KFMASH system indicates a univariant assemblage. It may be noted that this sample is collected close to the staurolite isograd on the low temperature side as expected.

Table 2
Temperatures estimated for M2 metamorphic event at $P = 5500$ bar from core compositions of co-existing minerals

Sample	Garnet–Biotite (Ferry and Spear', 1978 with Mn, Ca correction Ganguly and Saxena, 1984)	Garnet–Chlorite (Dickenson and Hewitt, 1986)	Garnet–Muscovite (Hynes and Forest, 1989)	Muscovite-Biotite (Hoisch, 1989)	Hornblende–Plagioclase (Holland and Blundy, 1994)
Garnet–Biotite–Chlorite zone/Kyanite–Chloritoid zone					
Dh 20	590, 530 °C, mean: 560 °C		580, 540 °C, mean: 560 °C	580, 540 °C, mean: 560 °C	
Kp 99	(500, 410 °C, mean: 555 °C)	580 °C, mean: 380 °C	550 °C	570 °C (470 °C)	
A 817		520 °C, mean: (480 °C)	550 °C		
K 65		520 °C, mean: 480 °C			
Kp 80	560 °C, (490 °C, 410, mean: 450 °C)		550 °C	620 °C	
A 810					540, 560 °C, mean: 550 °C
Staurolite–Biotite–zone/Staurolite–Garnet—Chlorite zone					
Kp 95	570, 590 °C°C, mean: 580 °C				
Kp 62	590, 550 °C, mean: 570 °CC	(450 °C)	590, 520, 550 °C, mean: 550 °C (490 °C)	530 °C (380 C°C)	
Kp 73	510 °C, mean: 460 °C			(400 °C)	
Kp 86					610, 590 °C, mean: 600 °C

Values in parantheses indicate estimated temperatures for M3 from rim compositions.

4.3. M3 metamorphism

M3 metamorphism encompassed local retrogression of garnet, staurolite and chloritoid into chlorite and muscovite. The flaky retrogression products show weak to prominent orientation parallel to the axial planes of D3 crenulations. No conversion of kyanite to andalusite or sillimanite is observed.

5. Metamorphic *P–T* conditions

5.1. M1 metamorphic event

The *P–T* condition during M1 metamorphism cannot be adequately constrained, but it must have been restricted to the andalusite stability field with an upper limit dictated by the appearance of chloritoid during M2.

5.2. M2 metamorphic event

The peak metamorphic condition during this event was in the stability fields of kyanite and staurolite. Fortunately, the mineral assemblages permit quantitative estimation of *P–T* from thermobarometry.

The temperature for M2 metamorphism has been computed at $P = 5.5$ kb from garnet–biotite, garnet–chlorite, garnet–muscovite and muscovite–biotite pairs in pelitic schists and from hornblende–plagioclase in intercalated amphibolites, using the formulations of Ganguly and Saxena (1984) for garnet–biotite pairs, Dickenson and Hewitt (1986) for garnet–chlorite pairs, Hynes and Forest (1988) for garnet–muscovite pairs, Hoisch (1989) for muscovite–biotite pairs and Holland and Blundy (1994) for hornblende–plagioclase pairs.

The temperatures obtained from the core compositions in the garnet-grade and staurolite-grade samples are overlapping and broadly converge at 520–590 °C, with a mean value of 550 ± 50 °C (Table 2). This is a lower limit of the peak temperature during M2 metamorphism and agrees well the experimental results of staurolite formation (Ganguly, 1968, 1969).

Pressures at this temperature were retrieved from the Fe-end member reaction for the assemblage garnet–muscovite–plagioclase–biotite

$$\text{almandine} + \text{grossular} + \text{muscovite} = 3\ \text{anorthite} + \text{annite}$$

The geobarometric formulations of Hodges and Spear (1982) and Hoisch (1990) were adopted in the retrieval calculations. Fe end-members were preferred over Mg end-members, because garnets in the samples are substantially richer in almandine compared to the pyrope component, and therefore errors arising out of extrapolation from Fe end-member reaction should be minimal. The computed pressures from the Fe end-member formulations of Hodges and Spear (1982) and Hoisch (1990) are summarized in Table 3. The values range from 3.8 to 7.4 kb in the garnet

Table 3
Pressure estimated from the reaction almandine + grossularite + muscovite = 3 anorthite + annite, at $T = 550$ °C (823 K)

Sample	Hodges and Spear (1982)	Hoisch (1990)
Garnet grade		
Kp 80	6.4–7.4 kb, mean: (6.8 kb)	6.0–6.7 kb, mean: (6.4 kb)
Dh 20	3.8–4.4 kb, mean: (3.9 kb)	4.4–4.6 kb, mean: (4.5 kb)
Kp 99	4.4–6.3 kb, mean: (5.3 kb)	5.8 kb
Staurolite grade		
Kp 62	4.6–5.9 kb, mean: (5.1 kb)	4.5–5.7 kb, mean: (4.9 kb)
Kp 73	5.5–5.7 kb, mean: (5.6 kb)	5.0–5.2 kb, mean: (5.1 kb)

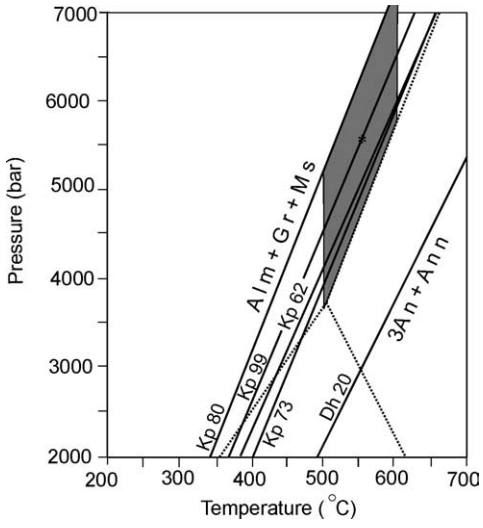

Fig. 8. Estimated *P–T* conditions (shaded area) for M2 metamorphic event. See text for discussion and Tables 2 and 3 for temperature and pressure estimates.

grade and 4.5–5.9 kb in the staurolite grade. The assemblages are kyanite-bearing and the minimum pressure for stabilizing kyanite at 550 °C is approximately 5.0 kb. Therefore, calculated pressures that are lower than this value are clearly erroneous. The actual pressure should therefore be limited within 5.0 and 7.4 kb (Hodges and Spear's 1982 formulation) and 5.0 and 6.7 kb (Hoisch's 1990 formulation). The range of *P–T* values for near-peak *P–T* conditions during M2 is shown as a stippled field in Fig. 8 with median values around 550 °C and 5.5 kb.

5.3. P_{H_2O} conditions during M2 metamorphism

An attempt has been made to constrain the X_{H_2O} conditions during M2 metamorphism. The reaction of choice for water barometry is taken to be

annite + muscovite + 3 quartz = 2 K-feldspar + almandine + 2 H_2O,

primarily because the activity composition relations of the constituent phases are well constrained (McMullin et al., 1991; Berman and Koziol, 1991; Fuhrman and Lindsley, 1988), and the assemblage of biotite–muscovite–garnet–K-feldspar–quartz is present in low aluminous and calcareous pelites. The absence of biotite in HAP precludes estimation of X_{H_2O} in these rocks.

The *P–T* locations of the reaction at X_{H_2O} conditions between 0.1 and 1.0 are shown in Fig. 9 for low aluminous pelites, (sample nos. Kp62 and Dh20). The computations were done using the TWEEQU (Thermobarometry With Estimation of Equilibration state) program of Berman (1992), with activity composition relations of the relevant phases built into the program (biotite—McMullin et al., 1991, muscovite—Chatterjee and Froese, 1975; garnet—Berman, 1990; Berman and Koziol, 1991). In the computations, the K-feldspar activity was taken to be unity.

It is evident from Fig. 9 that for Kp62 and Dh20, the *P–T* conditions are satisfied for a wide range of X_{H_2O} values. For Kp62, the best convergence for all Mg and Fe end-member reactions involving garnet, biotite, plagioclase, quartz, K-feldspar and fluid in the system CaO–MgO–FeO–Al_2O_3–SiO_2–K_2O–H_2O–CO_2 is achieved for $X_{H_2O} = 0.25$ ($CO_2 = 0.75$), $T = 540$ °C and P around 4.8 kb (Fig. 10b). Mg and Fe end members of chlorite and staurolite were not included in the computation because the relationships among values of X for these phases are ill-constrained.

In calcareous pelite (Kp 80), the M2 *P–T* conditions are satisfied for a large range of X_{H_2O} values, ($X_{H_2O} \geq 0.4$) (Fig. 10a). While the convergence among Mg end-member reactions involving biotite, muscovite, garnet, K-feldspar, quartz is poor, the Fe end-member reactions for the phases converge adequately over a large range of $P - T - X_{H_2O}$

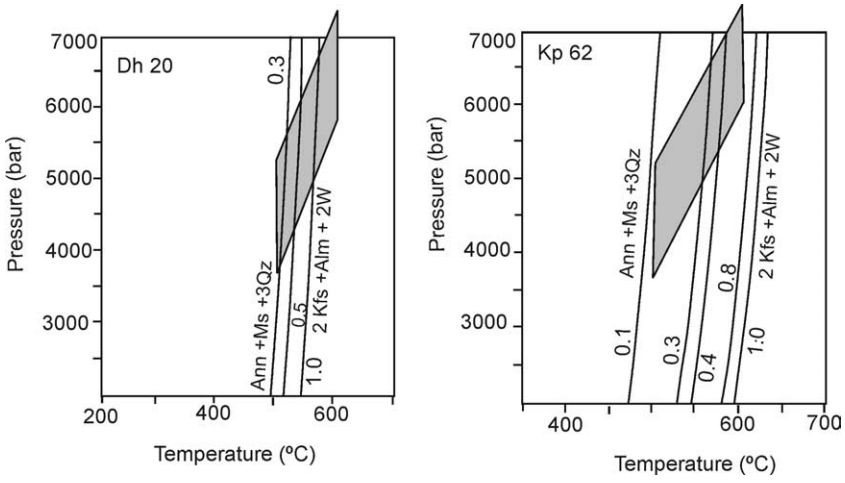

Fig. 9. *P–T* location of the reaction curves for annite + muscovite + 3 quartz = 2 K-feldspar + almandine + 2 H_2O at X_{H_2O} conditions, between 0.1 and 1.0, for samples Kp62 (HAP) and Dh20 (LAP). Shaded parallelogram is the estimated *P–T* field as shown in Fig. 8.

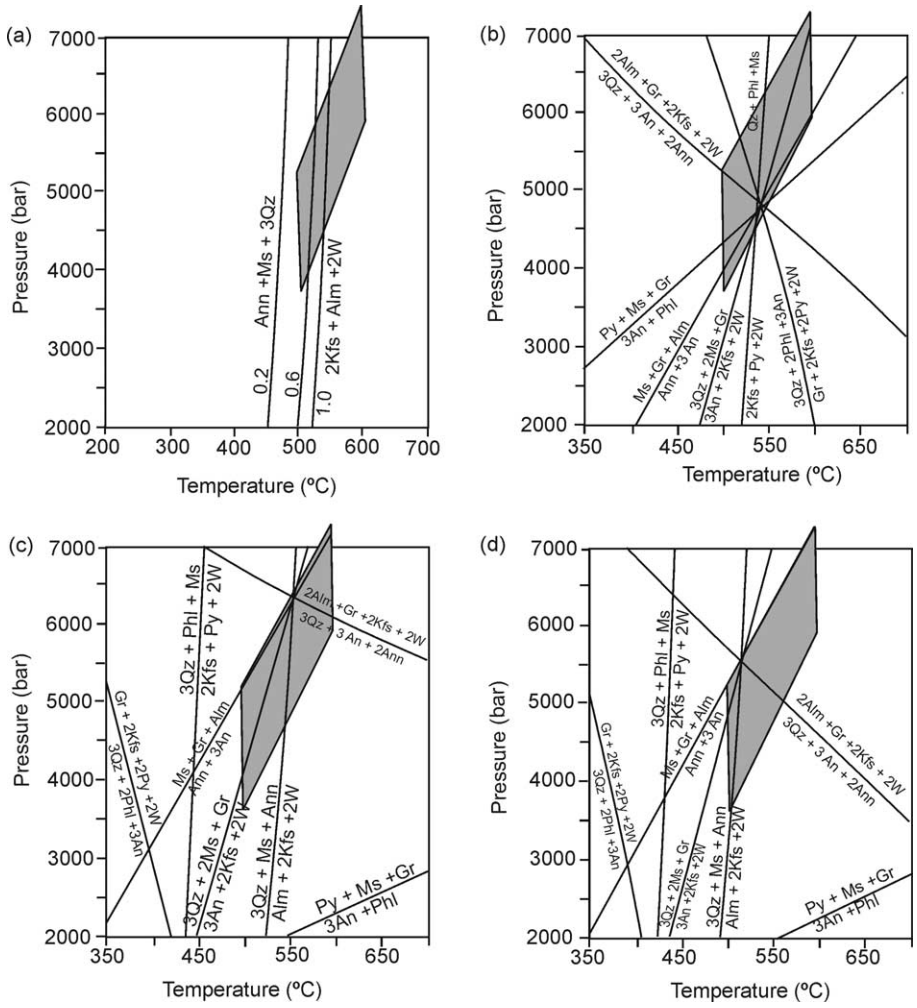

Fig. 10. (a) *P–T* location of the reaction curves for annite + muscovite + 3 quartz = 2 K-feldspar + almandine + 2 H_2O at varying X_{H_2O} (0.2, 0.6 and 1.0) for Sample Kp80 (calcareous pelite). (b) Convergence of Fe end-member reactions at $X_{H_2O} = 0.25$ for Sample Kp62. (c) Convergence of Fe end-member reactions at $X_{H_2O} = 0.9$ for Sample Kp80. (d) Convergence for Fe end-member reactions at $X_{H_2O} = 0.35$ for Sample Kp80. The shaded parallelogram is the estimated *P–T* field as shown in Fig. 8.

conditions: 6.4 kb, 560 °C, 0.9 and 5.6 kb, 520 °C, 0.35 (Fig. 10c and d).

It appears from the above discussion that X_{H_2O} in the low aluminous pelites and calcareous pelites was unlikely to have been identical or similar. This non-uniformity in estimated X_{H_2O} values suggests that the fluid composition in rocks prior to and during M2 metamorphism was buffered, and any fluid influx that may have occurred was not extensive enough to overcome the buffering capacity of the rocks.

5.4. M3 metamorphic event

The absence of post-D2 andalusite/sillimanite in the study-area indicates that the metamorphic *P–T* condition during M3 was limited by the stability field of kyanite. Additionally, the retrogressive stabilization of chlorite at the expense of M2 staurolite and garnet suggests that the M3 metamorphic conditions corresponded to greenschist facies conditions. The estimated temperatures from the rim compositions of garnet and retrogressed chlorite/muscovite/biotite are low and consistent with the above observation. For example, garnet–biotite pairs register temperatures between 410 and 500 °C for both garnet-zone and staurolite-zone samples. Similar low temperatures are retrieved from garnet–chlorite (380–480 °C), muscovite–biotite (380–470 °C) and garnet–muscovite (ca. 490 °C) assemblages. The retrograde assemblages are not amenable to quantitative geobarometry, and hence pressures could not be estimated for the M3 metamorphic event.

6. Pressure–temperature trajectory

The textural relations and the inferred reactions can now be interpreted in terms of the relevant petrogenetic grid in order to constrain the geodynamic evolution of the North Singhbhum Fold Belt (NSFB). The observed phases,

staurolite, garnet, kyanite, chloritoid, muscovite, chlorite, quartz and vapour can be adequately represented in the system KFMASH (see Spear and Cheney, 1989; Powell and Holland, 1990; Droop and Harte, 1995 and the references cited therein). However, there exists a debate about the relative stabilities of chloritoid + biotite and garnet + chlorite assemblages, which led to the formulation of two contrasting topologies around the [Al_2SiO_5, Crd] invariant point (Droop and Harte, 1995). Biotite is absent in chloritoid-bearing assemblages in the HAP rocks of the study area, but kyanite is present and the observed assemblages indicate stability of biotite-free assemblages. Stuwe and Ehlers (1997), using the database of Holland and Powell (1990), constructed a *P–T* grid depicting the stability of the degenerate invariant point [bi, mu] and linked it with the [cld] invariant point.

A chemographically valid and topologically correct arrangement of the reactions in the KFMASH system around the invariant points [bi], [cld] and [and] has been constructed following Schreinemakers rules and is presented in Fig. 11. The phases considered are those observed in the study area: quartz (qtz), muscovite (mu), biotite (bi), chlorite (chl), chloritoid (cld), garnet (grt), staurolite (st), andalusite/kyanite/sillimanite (and/ky/sil). In this figure we considered the invariant points [bi], [cld] and [and] to be stable; all the assemblages also contain qtz + mu + H_2O.

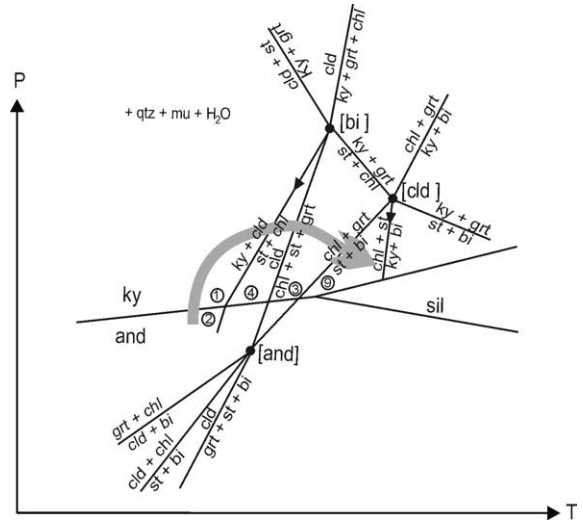

Fig. 11. Constructed partial Schreinemakers net for the KFMASH system with the phases quartz (qtz), muscovite (mu), biotite (bi), chlorite (chl), chloritoid (cld), garnet (gt), staurolite (st) and andalusite–kyanite–sillimanite (and/ky/sil) and H_2O. Univariant reaction curves involving AFM mineral phases around invariant points [bi], [cld] and [and] are shown. All assemblages contain qtz + mu + H_2O as additional phases. Filled arrows indicate the directions in which the invariant points would be displaced by addition of components MnO and CaO. Stability fields of andalusite, kyanite and sillimanite are also shown. The schematic positions of M1 and M2 assemblages are marked. M1—and + chl, 1—chl + cld + ky (M2, HAP), 4—chl + ky + st (M2, HAP), 3—gt + chl + st (M2, HAP), 9—bi + gt + st (M2, LAP). The numbers correspond to the assemblages in Table 1. Possible *P–T* trajectory is shown by the thick line.

Depending on the relative *P–T* stability of grt + chl and cld + bi, two contrasting topologies around the [Al_2SiO_5] invariant point have been proposed (Harte and Hudson, 1979, Spear and Cheney, 1989). As biotite is absent in the chloritoid-bearing rocks of the study area, the choice of [Al_2SiO_5] topology is not expected to affect the overall phase relations in these rocks. We have accepted Harte and Hudson's (1979) topology around the [Al_2SiO_5] invariant point. The [cld] invariant point is placed at a lower pressure than [bi], which is consistent with the grid proposed by Powell and Holland (1990).

Addition of MnO + CaO in the system KFMASH system will increase the variance of the system and will cause displacement of the invariants along their respective garnet-absent univariant reaction curves. This is shown by the filled arrow-heads in Fig. 11. The net effect would be to enlarge the stability field of garnet-bearing assemblages at the cost of chloritoid-bearing assemblages.

The textural relations in the HAP rocks of the present area suggest that andalusite + chlorite stabilized early. This is the earliest recognizable metamorphic assemblage and is termed M1. As mentioned earlier, the *P–T* conditions of M1 metamorphism could not be precisely constrained; the indicated position of M1 in the *P–T* field in Fig. 11 is only approximate. The textural relations further demonstrate that the M1 assemblage was unstable during the imposition of the more intense M2 metamorphism that led to the stabilization of the diverse porphyroblastic phases. The early part of M2 metamorphism was characterized by instability of andalusite in favour of kyanite, possibly through the Carmichael-type ionic reaction (Carmichael, 1969). Chloritoid formed soon after the alteration of andalusite. According to the petrogenetic grid presented in Fig. 11, the stabilization of kyanite + chloritoid over andalusite + chlorite calls for an increase in pressure. The staurolite bearing assemblages developed after kyanite + chloritoid. The topological relations suggest an increase of temperature for the stabilization of staurolite. The suggested positions of three staurolite-bearing assemblages in the HAP and LAP schists are shown in Fig. 11. These plots show that when going from M1 to M2, the *P–T* trajectory follows a clockwise path. Since the *P–T* conditions of M3 metamorphism could not be precisely constrained, the nature of the *P–T* path beyond the peak M2 condition remains uncertain.

7. Discussion

The proposed *P–T* trajectory lends support to the model of initial rifting followed by compressional tectonics (Mukhopadhyay, 1990). The earliest metamorphic event (M1), characterized by stabilization of greenschist facies mineralogy (muscovite, chlorite, biotite and andalusite), essentially preceded the folding events. Tectonic models proposed for the NSFB envision that it developed either as an ensialic basin (Gupta et al., 1980; Mukhopadhyay, 1984;

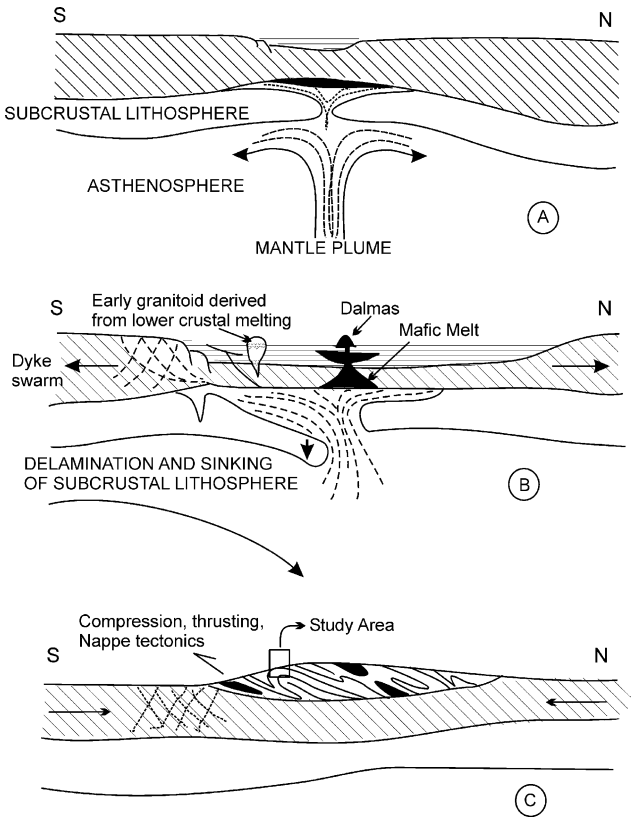

Fig. 12. Tectonic model for the evolution of the North Singhbhum Fold Belt as an ensialic orogenic belt (adapted from Kröner, 1981; Mukhopadhyay, 1990). Position of the study area is shown in the figure.

Gupta and Basu, 2000) (Fig. 12) or as a marginal basin (Bose and Chakraborti, 1981). Both models invoke initial stage of rifting. The presence of a long belt of mafic volcanics (Dalma volcanics) (Fig. 3) in the stratigraphic sequence testifies to the thermal perturbation in the initial stage of evolution of the belt. We interpret that asthenospheric upwelling that led to extension and basin formation was responsible for the pre-orogenic heating at low pressure, leading to the M1 metamorphism (cf. Wickham and Oxburgh, 1987; Robinson et al., 1999). However, the temperature at this stage did not rise very high and the metamorphism did not go beyond the greenschist facies.

This was followed by folding and thrusting events (cf. Kröner, 1981). Detailed structural studies in different parts of the belt (Ghosh and Sengupta, 1987; 1990; Mukhopadhyay and Deb, 1995; Mukhopadhyay et al., 2004) have confirmed that the shearing and thrusting started quite early in the deformation history and continued during the later stages. Loading caused by thrust stacking (Sengupta and Mukhopadhyay, 2000) led to increased pressure and a rise in temperature, causing widespread growth of porphyroblastic garnet, kyanite and staurolite in the amphibolite facies during M2 metamorphism. As discussed by England and Thomson (1984) and Spear (1993), a clockwise *P–T* path is expected in this tectonic scenario. It may be noted that in the area of study, the temperature during the early rifting (M1) did not rise very high, and the subsequent metamorphism was not of the nature of near isothermal increase of pressure followed by isobaric cooling, which would have given rise to an anti-clockwise *P–T* path (Appel et al., 1998; Baba, 1998; Abati et al., 2003). On the contrary, the orogenic loading caused a rise in both *P* and *T* and was responsible for the clockwise *P–T* path.

Large scale warping during D3 was synchronous with retrogression of the M2 porphyroblasts to chlorite, muscovite and biotite at greenschist facies conditions (M3). This is indicated by the occurrence of M3 minerals that are stable in the fabric generated by D3 deformation. This final stage of metamorphism is attributed to cooling and hydration of the rocks (downgradation), synchronous with exhumation related either to tectonic denudation or erosional unroofing. However, structures associated with tectonic denudation are not observed and the absence of sillimanite in the pelitic rocks precludes post-peak isothermal decompression.

Thermodynamic analyses of dehydration reactions in pelitic rocks indicate that the estimated X_{H_2O} values for low aluminous pelites and calcareous pelites were not identical. This suggests that fluid composition in rocks before and during M2 metamorphism was buffered and that fluid influx, if any, was not extensive enough to overcome the buffering capacity of the rocks. Thus the pelitic rocks, during M2 metamorphism, behaved as closed systems with respect to fluids.

The tectono-metamorphic model suggested here indicates evolution of the CITZ as a compressional orogenic belt with an initial history of rifting, at least in the section adjacent to the Singhbhum cratonic nucleus. The initial continental rifting led to generation of oceanic crust that is now represented by the MORB-like Dalma Volcanics (Bose, 1994). The abundance of volcanic and volcaniclastic rocks in the supracrustal sequence argues against a passive margin setting for the basin. However, the evidence gathered does not conclusively indicate whether the basin originated through ensialic orogenesis or developed in an active continental margin setting.

8. Conclusions

The Proterozoic fold belt rocks of North Singhbhum are characterized by three deformation events (D_1, D_2 and D_3) and M_1, M_2 and M_3 metamorphism. M_1 metamorphism (pre-D1) is characterized by the greenschist facies minerals muscovite, chlorite, biotite and andalusite, while chloritoid, kyanite, garnet and staurolite porphyroblasts were stabilized during M_2 metamorphism that post dated D_2. The near-peak *P–T* conditions during D_2 were ~550 °C and 5.5 kbar. The retrogressive M3 metamorphism stabilized chlorite at the expense of M2 staurolite and garnet. The *P–T* trajectory reconstructed for the three metamorphic events is consistent with a tectonic model of initial rifting followed by crustal shortening (cf. Mukhopadhyay, 1990).

9. Uncited references

Dickenson and Hewitt (1991), Holdaway et al. (1988), Sarkar and Mukherjee (1958).

Acknowledgements

Financial help was received from the University Grants Commission, India, and the Indian National Science Academy for the work. We are grateful to Prof. Abhijit Bhattacharya for many helpful suggestions on the analysis of data. Dr H.K. Gupta gave the permission to use the EPMA at NGRI, Hyderabad, and Prof. S. Dasgupta carried out the EPMA analyses of a few samples at the University of Bonn. Dr A. Chattopadhyay helped us during fieldwork and permitted us to use some of the structural data collected by him. We thank Ms Sudeshna Banerjee and Ms Kakoli Mukherjee for their contribution in this work. We have been benefitted by the constructive comments of Dr A. Roy and an anonymous reviewer.

Appendix A. Electronprobe microanalytical data and structural formulae of representative minerals used in computations

A.1. Garnet

	HAP Schist		LAP Schist		Impure carbonate	
	Core	Rim	Core	Rim	Core	Rim
SiO_2	37.40–37.41	37.16–37.32	36.48–39.93	36.36–39.66	36.49–37.08	36.21–36.98
TiO_2	0.04–0.07	0.02–0.04	0.00–0.07	0.00–0.08	0.06–0.27	0.09–0.12
Al_2O_3	21.11–21.82	21.69–21.72	19.28–22.53	20.16–21.89	21.24–21.80	21.53–21.96
FeO(t)	28.41–29.45	28.37–31.00	30.49–37.48	30.82–36.56	26.82–28.09	30.21–30.85
MnO	7.14–7.85	5.21–7.49	2.09–8.41	1.03–7.87	7.38–7.90	4.65–4.72
MgO	1.95–2.07	2.06–2.18	0.69–2.53	0.75–2.43	1.60–1.75	2.28–2.30
CaO	2.74–2.92	2.68–2.88	1.53–3.64	1.62–3.63	4.30–4.62	3.49–3.76
Na_2O	0.00–0.20	0.00–0.09	0.00–0.09	0.00–0.20	0.01–0.16	0.05–0.10
K_2O	0.02–0.05	0.03–0.06	0.00–0.07	0.00–0.05	0.04–0.08	0.04–0.05
Cr_2O_3	0.00–0.07	0.00	0.00–0.07	0.00–0.12	0.00–0.08	0.00–0.05
Si	2.99–3.01	2.99–3.00	2.95–3.14	2.98–3.13	2.96–2.98	2.93–2.98
Ti	0.00	0.00	0.00	0.00	0.00–0.02	0.01
Al(iv)	0.00–0.01	0.00–0.01	0.00–0.05	0.00–0.02	0.02–0.04	0.02–0.07
Al(vi)	2.00–2.05	2.04–2.06	1.88–2.06	1.91–2.06	2.01–2.02	2.02–2.03
Fe^{2+}	1.90–1.98	1.91–2.08	1.99–2.54	2.03–2.50	1.80–1.89	2.04–2.08
Fe^{3+}	0.00	0.00	0.00–0.12	0.00–0.09	0.00–0.11	0.00
Mn	0.49–0.53	0.35–0.51	0.14–0.59	0.07–0.54	0.50–0.54	0.32
Mg	0.23–0.25	0.25–0.26	0.09–0.31	0.09–0.29	0.19–0.21	0.27–0.28
Ca	0.24–0.25	0.23–0.25	0.13–0.32	0.14–0.32	0.37–0.40	0.30–0.32
Na	0.00–0.03	0.00–0.01	0.00–0.01	0.00–0.03	0.00–0.02	0.01–0.02
K	0.00–0.01	0.00–0.01	0.00–0.01	0.00	0.00–0.01	0.00–0.02
Cr	0.00	0.00	0.00	0.00–0.01	0.00–0.01	0.00
Fe/Mg	7.98–8.18	7.73–7.98	7.67–27.11	7.28–25.00	8.60–9.85	7.44–7.53

Representative analytical data of garnet and structural formulae calculated on the basis of 12 oxygens.

A.2. Plagioclase

	LAP-Schist		Impure carbonate		Metabasic	
	Core	Rim	Core	Rim	Core	Rim
SiO_2	59.98–62.99	61.81–62.97	6.83–62.42	57.78–58.56	53.28–53.98	51.24–54.93
TiO_2	0.00–0.01	0.00–0.02	0.00	0.00–0.03	0.02–0.04	0.02–0.04
Al_2O_3	23.12–24.86	23.35–24.40	24.94–25.97	26.92–27.24	29.65–30.81	29.46–32.15
FeO(t)	0.00–0.05	0.00–0.14	0.08–0.12	0.07–0.23	0.10–0.23	0.06–0.15
MnO	0.00–0.07	0.00	0.01	0.00–0.09	0.00	0.01–0.03
MgO	0.00–0.01	0.00	0.01	0.00–0.02	0.00–0.05	0.00–0.05
CaO	4.42–5.78	4.95–6.09	5.94–14.87	7.30–7.37	9.98–11.48	10.07–11.86
Na_2O	7.34–8.61	7.48–9.23	7.39–8.14	6.35–6.85	4.91–5.19	4.46–5.21

(*continued on next page*)

	LAP-Schist		Impure carbonate		Metabasic	
	Core	Rim	Core	Rim	Core	Rim
K_2O	0.06–0.11	0.06–0.08	0.12–0.16	0.09–0.12	0.06–0.07	0.03–0.08
Cr_2O_3	0.00	0.07–0.08	0.00–0.06	0.00–0.01	0.00	0.00–0.01
NiO	0.00–0.05	0.00–0.10	0.00–0.01	0.00–0.01	0.00–0.02	0.00–0.02
Si	2.73–2.81		2.59–2.68	2.60–2.61	2.41–2.43	2.34–2.47
Ti	0.00		0.00	0.00	0.00	0.00
Al(t)	1.22–1.30		1.22–1.35	1.43	1.60–1.63	1.56–1.70
Fe^{2+}	0.00		0.00	0.00–0.01	0.00–0.01	0.00–0.01
Mn	0.00		0.00	0.00	0.00	0.00
Mg	0.00		0.00	0.00	0.00	0.00
Ca	0.21		0.22–0.28	0.35	0.50–0.53	0.48–0.58
Na	0.63–0.75		0.63–0.65	0.56–0.59	0.42–0.46	0.36–0.45
K	0.00–0.01		0.01	0.01	0.00	0.00
Cr	0.00		0.00	0.00	0.00	0.00
Ni	0.00		0.00	0.00	0.00	0.00
Xan	0.24–0.29		0.25–0.31	0.37–0.39	0.51–0.55	0.51–0.61
Xab	0.70–0.76		0.69–0.74	0.61–0.62	0.44–0.48	0.39–0.48

Representative analytical data of plagioclase and structural formulae calculated on the basis of eight oxygens.

A.3. Biotite

	LAP Schist		Impure carbonate	
	Core	Rim	Core	Rim
SiO_2	37.52–38.60	37.75–38.06	35.50–36.45	35.27–36.40
TiO_2	1.17–1.28	1.17–1.37	1.27–1.44	1.17–1.61
Al_2O_3	19.25–19.78	19.04–19.73	20.03–20.18	19.37–20.76
FeO(t)	17.15–17.59	16.91–18.08	18.06–19.61	17.73–18.77
MnO	0.04–0.12	0.00–0.03	0.00–0.02	0.00–0.01
MgO	10.26–10.8–48	10.44–10.67	10.85–10.90	11.07–11.58
CaO	0.00–0.10	0.00–0.09	0.00–0.01	0.00
Na_2O	0.17–0.40	0.18–0.33	0.18–0.28	0.13–0.34
K_2O	0.81–0.82	0.79–0.82	8.50–8.77	8.76–9.19
Cr_2O_3	0.01–0.05	0.00–0.07	0.01–0.06	0.03–0.04
NiO	0.00–0.05	0.05–0.08	0.00	0.00–0.01
Si	2.79–2.85	2.80–2.84	2.65–2.72	2.63–2.72
Ti	0.07	0.07–0.08	0.07–0.08	0.07–0.09
Al(iv)	1.15–1.21	1.16–1.20	1.28–1.35	1.28–1.38
Al(vi)	0.52–0.54	0.50–0.53	0.43–0.48	0.43–0.45
Fe^{2+}	1.06–1.09	1.05–1.12	1.13–1.19	1.10–1.18
Mn	0.00–0.01	0.00	0.00	0.00
Mg	1.13–1.16	1.16	1.21–1.22	1.24–1.28
Ca	0.00–0.01	1.18	0.00	0.00
Na	0.02–0.06	0.00–0.01	0.03–0.04	0.02–0.05
K	0.81–0.82	0.03–0.05	0.81–0.84	0.84–0.87
Cr	0.00	0.80–0.82	0.00	0.00
Ni	0.00	0.00	0.00	0.00
XFe	0.48–0.49	0.47–0.49	0.48–0.50	0.46–0.49

Representative analytical data of biotite and structural formulae calculated on the basis of 11 oxygens.

A.4. Muscovite

	HAP-Schist		LAP-Schist		Impure carbonate	
	Core	Rim	Core	Rim	Core	Rim
SiO_2	46.48–48.89	46.14–48.71	47.31–48.92	45.94–48.08	50.35	46.84
TiO_2	35.29–37.01	35.28–40.33	34.29–36.29	31.33–35.09	29.58	0.48
Al_2O_3	0.14–0.27	0.00–0.31	0.20–0.26	0.22–0.45	0.34	29.57

	HAP-Schist		LAP-Schist		Impure carbonate	
	Core	Rim	Core	Rim	Core	Rim
FeO(t)	1.58–2.13	0.70–2.46	1.81–2.29	1.62–3.27	3.58	4.01
MnO	0.00–0.05	0.00–0.06	0.00–0.06	0.00	0.00	0.05
MgO	0.20–0.46	0.00–0.53	0.55–0.82	0.54–0.65	1.45	2.59
CaO	0.00–0.17	0.00–0.74	0.00	0.00–0.01	0.74	0.07
Na_2O	1.61–3.19	1.81–6.37	0.74–1.07	0.52–1.37	2.21	0.19
K_2O	5.94–8.42	0.46–8.25	7.53–9.03	8.97–10.82	9.25	10.95
Cr_2O_3	0.01–0.10	0.03–0.12	0.00–0.08	0.00	0.00	0.00
Si	3.04–3.18	2.99–3.13	3.11–3.16	3.16–3.19	3.31	3.20
Al(iv)	0.82–0.94	0.87–1.01	0.85–0.89	0.82–0.84	0.69	0.81
Al(vi)	1.87–1.92	1.86–2.00	1.84–1.94	1.74–1.85	1.60	1.58
Ti	0.01	0.00–0.01	0.01	0.01–0.03	0.02	0.03
Fe^{2+}	0.09–0.12	0.04–0.14	0.08–0.12	0.08–0.19	0.20	0.23
Mn	0.00	0.00	0.00–0.01	0.00	0.00	0.01
Mg	0.02–0.05	0.00–0.05	0.04–0.08	0.04–0.07	0.14	0.27
Ca	0.00	0.00–0.05	0.00	0.00	0.55	0.01
Na	0.21–0.40	0.17–0.78	0.08–0.16	0.05–0.16	0.28	0.03
K	0.49–0.71	0.06–0.68	0.62–0.79	0.79–0.96	0.78	0.96
Cr	0.00	0.00–0.01	0.00–0.01	0.00	0.00	0.00

Representative analytical data of muscovite and structural formulae calculated on the basis of 11 oxygens.

A.5. Amphibole

	Metabasic rock	
	Core	Rim
SiO_2	44.05–45.37	43.36–45.13
TiO_2	0.39–0.41	0.39–0.45
Al_2O_3	14.01–14.99	14.64–16.10
FeO(t)	14.51–15.20	13.98–15.35
MnO	0.25–0.36	0.16–0.25
MgO	10.86–11.16	9.27–11.12
CaO	10.33–10.68	10.37–10.52
Na_2O	1.36–1.51	1.51–1.60
K_2O	0.34–0.36	0.32–0.42
Cr_2O_3	0.00–0.06	0.06–0.12
NiO	0.00–0.02	0.01–0.04
Si	6.36–6.60	6.31–6.56
Ti	0.09–0.87	0.09
Al(t)	2.43–2.62	2.44–2.81
Fe^{2+}	1.74–1.83	1.74–1.84
Mn	0.04	0.02–0.04
Mg	2.34–2.53	2.01–2.44
Ca	1.57–1.65	1.66
Na	0.35–0.39	0.35–0.53
K	0.07–0.69	0.05–0.17
Cr	0.00–0.01	0.01–0.02
Ni	0.00	0.00

Representative analytical data of amphibole and structural formulae calculated on the basis of 23 oxygens.

A.6. Chlorite

	HAP Schist		LAP Schist		Metabasic rock	
	Core	Rim	Core	Rim	Core	Rim
SiO_2	23.93–27.52	24.03–26.52	28.17–28.26	22.31–23.70	26.97–27.68	26.22–26.34
TiO_2	0.01–0.14	0.02–0.13	0.09	0.04–0.11	0.05–0.09	0.06–0.07

(*continued on next page*)

	HAP Schist		LAP Schist		Metabasic rock	
	Core	Rim	Core	Rim	Core	Rim
Al_2O_3	23.16–24.69	22.98–24.64	22.26–22.91	21.42–22.36	22.56–23.06	19.79–19.84
FeO(t)	17.96–25.42	18.27–23.94	21.13–21.48	29.32–31.50	16.77–17.09	18.07–17.85
MnO	0.12–0.29	0.10–0.33	0.04–0.10	0.00–0.11	0.18–0.28	0.15–0.28
MgO	14.01–18.37	13.20–17.51	14.83–15.70	10.63–11.50	19.61–20.44	18.50–18.91
CaO	0.00–0.09	0.00–0.11	0.02	0.00–0.04	0.03–0.16	0.08–0.12
Na_2O	0.00–0.15	0.00–0.40	0.00–0.01	0.00–0.34	0.00–0.07	0.00–0.11
K_2O	0.00–0.29	0.03–0.35	0.10–0.22	0.00–0.07	0.04–0.09	0.00–0.03
Cr_2O_3	0.00–0.10	0.00–0.04	0.00	0.00	0.04–0.13	0.00
NiO	0.04–0.09	0.00–0.11	0.00–0.13	0.00	0.04–0.06	0.00
Si	2.50–2.80	2.51–2.80	2.87–2.88	2.46–2.57	2.71–2.72	2.80–2.82
Ti	0.00–0.01	0.00–0.01	0.01	0.00–0.01	0.00–0.01	0.01
Al(iv)	0.20–1.50	1.30–1.49	1.12–1.13	1.39–1.54	1.23–1.29	1.18–1.20
Al(vi)	1.46–1.61	1.52–1.79	1.45–1.55	0.83–1.00	1.23–1.29	1.09–1.14
Fe^{2+}	1.51–2.21	1.56–2.14	1.80–1.83	2.71–2.88	1.40–1.44	1.60–1.62
Mn	0.01–0.03	0.01–0.03	0.00–0.01	0.00–0.01	0.02	0.01–0.03
Mg	2.17–2.71	2.01–2.66	2.25–2.39	1.76–1.89	2.93–3.03	2.95–3.01
Ca	0.00–0.01	0.00–0.01	0.00	0.00–0.01	0.01–0.02	0.01
Na	0.00–0.03	0.00–0.08	0.00	0.00–0.07	0.00–0.01	0.00–0.02
K	0.00–0.04	0.00–0.05	0.01–0.03	0.00–0.01	0.01	0.00
Cr	0.00–0.01	0.00	0.00	0.00	0.00–0.01	0.00
Ni	0.00–0.01	0.00–0.01	0.00–0.01	0.00	0.00–0.01	0.00
XFe	0.36–0.50	0.37–0.50	0.43–0.45	0.60–0.61	0.32	0.35

Representative analytical data of chlorite and structural formulae calculated on the basis of 14 oxygens.

A.7. Staurolite

	HAP-Schist		LAP-Schist		Impure carbonate	
	Core	Rim	Core	Rim	Core	Rim
SiO_2	28.79–29.62	28.90–29.38	28.86–29.63	28.11–29.68	27.78–28.00	27.11–28.00
TiO_2	0.40–0.48	0.42–0.47	0.45–0.63	0.36–0.43	0.50–0.66	0.46–0.58
Al_2O_3	54.47–54.64	54.06–54.61	53.78–53.82	53.98–54.71	53.69–54.05	53.20–54.07
FeO(t)	11.69–12.90	11.65–12.42	12.87–12.88	11.94–13.05	13.87–14.14	13.71–14.62
MnO	0.28–0.36	0.32–0.54	0.17–0.18	0.09–0.16	0.02–0.04	0.02–0.07
MgO	1.88–1.92	1.60–1.88	1.55–1.72	1.47–1.68	1.71–1.79	1.69–1.87
CaO	0.04–0.10	0.00–0.13	0.00–0.03	0.01–0.08	0.02	0.01–0.05
Na_2O	0.00	0.00–0.06	0.00	0.00	0.00–0.01	0.00
K_2O	0.04–0.05	0.03–0.06	0.05	0.03–0.05	0.03–0.04	0.02–0.06
Cr_2O_3	0.00–0.05	0.00–0.12	0.03–0.11	0.00–0.09	0.00–0.05	0.02–0.08
NiO	0.00–0.01	0.00–0.04	0.00	0.00–0.07	0.00–0.02	0.00
Si	7.84–8.06	7.90–8.01	7.95–8.08	7.74–8.12	7.70–7.73	7.54–7.75
Ti	0.08–0.10	0.09–0.10	0.09–0.13	0.07–0.09	0.10–0.14	0.10–0.12
Al(iv)	0.00–0.16	0.00–0.10	0.00–0.05	0.00–0.26	0.27–0.30	0.25–0.46
Al(vi)	17.37–17.47	17.45–17.53	17.29–17.40	17.45–17.49	17.22–17.28	17.15–17.29
Fe^{2+}	2.66–2.94	2.67–2.84	2.94–2.96	2.73–2.88	3.22–3.26	3.17–3.14
Mn	0.06–0.08	0.07–0.12	0.04	0.02–0.04	0.00–0.01	0.00–0.02
Mg	0.76–0.78	0.65–0.77	0.63–0.71	0.60–0.68	0.71–0.74	0.70–0.77
Ca	0.01–0.03	0.00–0.04	0.00–0.01	0.00–0.02	0.01	0.00–0.01
Na	0.00	0.00–0.03	0.00	0.00	0.00–0.01	0.00
K	0.01–0.02	0.01–0.02	0.02	0.01–0.02	0.01	0.01–0.02
Cr	0.00–0.01	0.00–0.03	0.01–0.02	0.00–0.02	0.00–0.01	0.00–0.02
Ni	0.00	0.00–0.01	0.00	0.00–0.02	0.00	0.00
XFe	0.77–0.79	0.78–0.81	0.81–0.82	0.81–0.83	0.82	0.80–0.83

Representative analytical data of plagioclase and structural formulae calculated on the basis of 48 oxygens.

A.8. Chloritoid

	HAP-Schist	
	Core	Rim
SiO_2	26.07–26.76	26.25
TiO_2	0.01–0.06	0.00
Al_2O_3	41.12–41.79	40.52
FeO(t)	20.17–21.20	21.53
MnO	0.56–0.70	0.58
MgO	3.24–3.38	3.34
CaO	0.01–0.03	0.03
Na_2O	0.02–0.14	0.06
K_2O	0.03–0.06	0.05
Cr_2O_3	0.01–0.10	0.03
NiO	0.02–0.09	0.09
Si	1.05–1.07	1.07
Ti	0.00–0.01	0.00
Al(t)	1.94–1.98	1.94
Fe^{2+}	0.68–0.72	0.73
Mn	0.02	0.02
Mg	0.20	0.20
Ca	0.00	0.00
Na	0.00	0.00
K	0.00	0.00
Cr	0.00	0.00
Ni	0.00	0.00
XFe	0.77–0.79	0.78

Representative analytical data of garnet and structural formulae calculated on the basis of 12 oxygens.

References

Abati, J., Arenas, R., Catalán, J.R.M., García, F.D., 2003. Anticlockwise *P–T* path of granulites from the Monte Castelo Gabbro (Órdenes Complex, NW Spain). Journal of Petrology 44, 305–327.

Acharyya, S.K., 2003. The nature of Mesoproterozoic Central Indian Tectonic Zone with exhumed and reworked older granulites. Gondwana Research 6, 197–214.

Appel, P., Möller, A., Schenk, V., 1998. High-pressure granulite facies metamorphism in the Pan-African belt of eastern Tanzania: *P–T–t* evidence against granulite formation by continent collision. Journal of Metamorphic Geology 16, 491–509.

Baba, S., 1998. Proterozoic anticlockwise *P–T* path of the Lewisian Complex of South Harris, Outer Hebrides, NW Scotland. Journal of Metamorphic Geology 16, 819–841.

Berman, R.G., 1990. Thermobarometry using multiequilibrium calculations: a new technique with petrologic applications. Canadian Mineralogist 29, 833–855.

Berman, R.G., Koziol, A.M., 1991. Ternary excess properties of grossular-pyrope-almandine garnets and their influence in geothermobarometry. American Mineralogist 76, 1223–1231.

Berman, R.G., 1992. TWEEQU (version 1.0). Thermobarometry with estimation of equilbrium state. http:\\www.gis.nrcan-gc.ca/twq.html.

Bose, M.K., 1994. Sedimentation pattern and tectonic evolution of the Proterozoic Singhbhum basin in the eastern Indian shield. Precambrian Research 231, 325–346.

Bose, M.K., Chakraborti, M.K., 1981. Fossil marginal basin from the Indian shield: a model for the evolution of the Singhbhum Precambrian belt, eastern India. Geologische Rundschau 70, 514–518.

Carmichael, D. M. 1969. On the mechanism of prograde metamorphic reactions in quartz-bearing pelitic rocks. Contributions to mineralogy and Petrology 20, 244–267.

Carmichael, D. M. 1970. Intersecting isograds in the Wheatstone lake Area Ontario. Journal of Petrology 11, 147–181.

Chakraborty, K., Sen, S.K., 1967. Regional metamorphism of pelitic rocks around Kandra, Singhbhum, Bihar. Contributions to Mineralogy and Petrology 16, 210–232.

Chattopadhyay, A., 1990. Structural and metamorphic evolution of the Precambrian rocks near Dhalbhumgarh, East Singhbhum. Unpublished PhD Thesis, University of Calcutta, pp. 1–150.

Dickenson, M.P., Hewitt, D., 1986. A garnet-chlorite geothermometer. Geological Society of America (Abstracts) 18, 584.

Droop, G.T.R., Harte, B., 1995. The effect of Mn on the phase relations of medium-grade pelites: constraints from natural assemblages on petrogenetic grid topology. Journal of Petrology 36, 1549–1578.

England, P.C., Thomson, A.B., 1984. Pressure–temperature–time paths of regional metamorphism I. Heat transfer during the evolution of regions of thickened continental crust. Journal of Petrology 25, 894–928.

Fuhrman, M.L., Lindsley, D.H., 1988. Ternary-feldspar modelling and thermometry. American Mineralogist 73, 201–216.

Ganguly, J. 1968. Analysis of stabilities of chloritoid and staurolite and some equilibria in the system FeO-Al_2O_3-SiO_2-H_2O-O_2. Journal of Science, 266, 277–298..

Ganguly, J. 1969. Chloritoid stability and related parageneses: theory, experiments and applications. American Journal of Science 267, 910–944.

Ganguly, J., Saxena, S.K., 1984. Mixing properties of aluminosilicate garnets: constraints from natural and experimental data, and applications to geothermobarometry. American Mineralogist 69, 87–97.

Ghosh, S.K., Sengupta, S., 1987. Structural history of the Singhbhum Shear Zone in relation to the northern belt, in: Saha, A.K. (Ed.), Geological evolution of Peninsular India—Petrological and Structural Aspects. Hindusthan Publishing Corporation, New Delhi, pp. 31–44.

Ghosh, S.K., Sengupta, S., 1990. Singhbhum Shear Zone: structural transition and a kinematic model. Proceedings of Indian Academy of Sciences (Earth and Planetary Sciences) 99, 229–247.

Gupta, A., Basu, A., 2000. North Singhbhum Proterozoic mobile belt, eastern India—a review. Geological Survey of India, Special Publication 55, 195–226.

Gupta, A., Basu, A., Ghosh, P.K., 1980. The Proterozoic ultramafic and mafic lavas and tuffs of the Dalma greenstone belt, Singhbhum, Eastern India. Canadian Journal of Earth Sciences 17, 210–231.

Harris, L.B., 1993. Correlation of tectonothermal events between the Central Indian Tectonic Zone and the Albany Mobile Belt of Western Austria, in: Findlay, R.H., Unrug, R., Banks, M.R., Veevers, J.J. (Eds.), Gondwana Eight: Assembly and Evolution and Dispersal. Balkema, Rotterdam, pp. 165–180.

Harris, L.B., Beeson, J., 1993. Gondwanaland significance of Lower Palaeozoic deformation in central India and SW Western Australia. Journal of Geological Society of London 150, 811–814.

Harte, B., Hudson, N.F.C. 1979. Pelite facies series and the temperatures and pressures of Dalradian metamorphism in eastern Scotland. In, The caledonides of the british Isles- reviewed. Geological Society of America.

Hodges, K.V., Spear, F.S., 1982. Geothermometry, geobarometry and the Al_2SiO_5 triple point at Mt. Moosilauke, New Hampshire. American Mineralogist 67, 1118–1134.

Hoisch, T.D., 1989. A muscovite–biotite geothrmometer. American Mineralogist 74, 565–572.

Hoisch, T.D., 1990. Emperical calibration of six geothermometers for the mineral assemblage quartz + muscovite + biotite + plagioclase + garnet. Contributions to Mineralogy and Petrology 104, 225–234.

Holland, T.J.B., 1979. Experimental determination of the reaction Paragonite = Jadeite + Kyanite + H_2O, and internally consistent thermodynamic data for part of the system Na_2O–Al_2O_3–SiO_2–H_2O, with application to eclogites and blueschists. Contributions to Mineralogy and Petrology 68, 292–301.

Holland, T., Blundy, J., 1994. Non-ideal interactions in calcic amphiboles and their bearing on amphibole–plagioclase thermometry. Contributions to Mineralogy and Petrology 108, 433–447.

Holland, T.J.B., Powell, R., 1990. An enlarged and updated internally consistent thermodynamic dataset with uncertainities and correlations: the system K_2O–Na_2O–CaO–MgO–MnO–FeO–Fe_2O_3–Al_2O_3–TiO_2–SiO_2–C–H_2–O_2. Journal of Metamorphic Geology 8, 89–124.

Hoschek, G., 1967. Untersuchungen zum stabilitätsbereich von chloritoid und staurolith. Contributions to Mineralogy and Petrology, 14, 123–162.

Hoschek, G., 1969. The stability of staurolite and chloritoid and their significance in metamorphism of pelitic rocks. Contributions to Mineralogy and Petrology 22, 208–232.

Hynes, A., Forest, R.C., 1988. Emperical garnet-muscovite geothermometry in low grade metapelites, Selwyn Range (Canadian Rockies). Journal of Metamorphic Geology 6, 297–309.

Jain, S.C., Nair, K.K.K., Yedekar, D.B., 1995. Geology of the Son–Narmada–Tapti lineament zone in Central India, Geological Survey of India, Special Publication, vol. 10 1995 pp. 1–154.

Kerrick, D.M., 1990. The Al_2SiO_5 Polymorphs. Reviews in Mineralogy, vol. 22. Mineralogical Society of America, Washington pp. 1–405.

KrishnaRao, N., Aggarwal, S.K., Rao, G.V.U., 1979. Lead isotopic ratios of uraninites and the age of uranium mineralisation in Singhbhum shear zone, Bihar. Journal of Geological Society of India 20, 124–127.

Kröner, A., 1981. Precambrian plate tectonics, in: Kröner, A. (Ed.), Precambrian Plate Tectonics. Elsevier, Amsterdam, pp. 57–90.

Kruhl, J.H., 1993. The *P–T–d* development at the basement–cover boundary in the north eastern Tauern Window (Eastern Alps): Alpine continental collision. Journal of Metamorphic Geology 11, 31–47.

McMullin, D., Berman, R.G., Greenwood, H.J., 1991. Calibration of the SGAM thermobarometer for pelitic rocks using data from phase equilibrium experiments and natural assemblages. Canadian Mineralogist 1991;, 29.

Miyashiro, A., 1973. Metamorphism and Metamorphic Belts. Gresham Press, London.

Mukhopadhyay, D., 1984. The Singhbhum shear zone and its place in the evolution of the Precambrian mobile belt, North Singhbhum. Indian Journal of Earth Sciences CEISM Seminar, 205–212.

Mukhopadhyay, D., 1990. Precambrian plate tectonics in the eastern Indian shield, in: Sychanthavong, S.P.H. (Ed.), Crustal Evolution and Orogeny. Oxford and IBH Publishing Co, New Delhi, pp. 71–100.

Mukhopadhyay, D., 2001. The Archaean nucleus of Singhbhum: the present state of knowledge. Gondwana Research 4, 307–318.

Mukhopadhyay, D., Deb, G., 1995. Structural and textural development in Singhbhum Shear zone, Eastern India. Proceedings of Indian Academy of Sciences (Earth and Planetary Sciences) 104, 385–405.

Mukhopadhyay, D., Sengupta, S., 1971. Structural geometry and time relation of metamorphic recrystallisation to deformation in the Precambrian rocks near Simulpal, Eastern India. Geological Society of America, Bulletin 82, 2251–2260.

Mukhopadhyay, D., Ghosh, M., Chattopadhyay, A.K., 2004. Structural pattern in the Dhalbhumgarh–Kokpara region and its bearing on the tectonics of the Proterozoic fold belt of North Singhbhum, Eastern India. Geological Survey of India, Special Publication 84, 43–60.

Naha, K., 1965. Metamorphism in relation to stratigraphy, structure and movements in part of East Singhbhum, Eastern India. Quarterly Journal of Geological, Mining and Metallurgical Society of India 37, 41–81.

Okuyama-Kusunose, 1994. Phase relations in andalusite–sillimanite type Fe-rich metapelites: tectonocontact metamorphic aureole north-east Japan. Journal of Metamorphic Geology 12, 153–168.

Passchier, C.W., Trouw, R.A.J., 1996. Micro-tectonics. Springer, Berlin pp. 1–289.

Powell, R., Holland, T., 1990. Calculated mineral equilibria in the pelite system, KFMASH (K_2O–FeO–MgO–Al_2O_3–SiO_2–H_2O). American Mineralogist 75, 367–380.

Radhakrishna, B.P., Naqvi, S.M., 1986. Precambrian continental crust of India and its evolution. Journal of Geology 94, 145–166.

Radhakrishna, B., Ramakrishnan, M., 1988. Archaean–Proterozoic boundary in India. Journal of Geological Society of India 32, 263–278.

Robinson, D., Reverdatto, V.V., Bevins, R.E., Polyansky, O.P., Sheplev, V.S., 1999. Thermal modeling of convergent and extensional tectonic settings for the development of low-grade metamorphism in the Welsh Basin. Journal of Geophysical Research (Solid Earth) 104, 23069–23080.

Roy, A., Hanuma Prasad, M., 2003. Tectonothermal events in Central Indian tectonic zone (CITZ) and its implications in Rodinian crustal assembly. Journal of Asian Earth Sciences 22, 115–129.

Sarakar, S.N., Saha, A.K., 1962. A revision of the Precambrian statigraphy and tectonics of Singhbhum and adjacent regions. Quarterly Journal of Geological, Mining and Metallurgical Society of India 34, 97–136.

Sarkar, S.N., Ghosh, D., Lambert, R.St.J., 1986. Rb–Sr and lead isotope studies on the soda granites from Mosaboni, Singhbhum Copper Belt, E. India. Indian Journal of Earth Sciences 13, 101–116.

Sengupta, S., Mukhopadhyay, P.K., 2000. Sequence of Precambrian Events in the Eastern Indian Craton, Geological Survey of India, Special Publication, vol. 57 2000 pp. 49–56.

Sengupta, S., Paul, D.K., Bishui, P.K., Gupta, S.N., Chakraborty, R., Sen, P., 1994. A geochemical and Rb–Sr isotopic study of Kuilapal granite and Arkasani granophyre from the eastern Indian craton. Indian Minerals 48, 77–88.

Spear, F.S., 1993. Metamorphic Phase Equilibria and Pressure–Temperature–Time Paths. Monograph. Mineralogical Society of America pp. 1–798.

Spear, F.S., Cheney, J.T., 1989. A petrogenetic grid for pelitic schists in the system SiO_2–Al_2O_3–FeO–MgO–K_2O–H_2O. Contributions to Mineralogy and Petrology 101, 149–164.

Stuwe, K., Ehlers, K., 1997. Multiple metamorphic events at Broken Hill, Australia. Evidence from chloritoid bearing paragenesis in the Nine-Mile Mine region. Journal of Petrology 38, 1167–1186.

Thomson, J.B., Norton, S.A. 1968. Paleozoic regional metamorphism inm New England and adjacent areas. In Zen, E-An, et al., (Eds.): Studies of Appalachian geology. Interscience Publishers. John Wiley, New York.

Tracy, R.J., 1982. Compositional zoning and inclusions in metamorphic minerals. Reviews in Mineralogy 10, 355–397.

Wang, P., Spear, F.S., 1991. A field and theoretical analysis of garnet + chloritoid + chlorite + biotite assemblages from the Tristate (MA, CT, NY) area, U.S.A. Contributions to Mineralogy and Petrology 106, 217–235.

Wickham, S.M., Oxburgh, E.R., 1987. Low-pressure regional metamorphism in the Pyrenees and its implications for the thermal evolution of rifted continental crust. Philosophical Transactions of Royal Society of London A321, 219–242.

Yardley, B., 1988. An Introduction to Metamorphic Petrology. Narosa Publishing House, New Delhi.

Yedekar, D.B., Jain, S.C., Nair, K.K.K., Dutta, K.K., 1990. The Central Indian Collision Suture, Geological Survey of India, Special Publication, vol. 28 1990 pp. 1–43.

Yoshida, M., 1995. Assembly of East Gondwanaland during the Mesoproterozoic and its rejuvenation during the Pan-African period, in: Yoshida, M., Santosh, M. (Eds.), India and Antarctica during the Precambrain Geological Society of India, Memoir, vol. 34, pp. 25–45.